The Astrophysical Journal, 780:72 (19pp), 2014 January 1 doi:10.1088/0004-637X/780/1/72
© 2014. The American Astronomical Society. All rights reserved. Printed in the U.S.A.

DISCOVERY OF POSSIBLE MOLECULAR COUNTERPARTS TO THE INFRARED DOUBLE HELIX NEBULA IN THE GALACTIC CENTER

R. Enokiya[1], K. Torii[1], M. Schultheis[2,3], Y. Asahina[4], R. Matsumoto[4], E. Furuhashi[1], K. Nakamura[1], K. Dobashi[5], S. Yoshiike[1], J. Sato[1], N. Furukawa[1], N. Moribe[1], A. Ohama[1], H. Sano[1], R. Okamoto[1], Y. Mori[1], N. Hanaoka[1], A. Nishimura[6], T. Hayakawa[1], T. Okuda[1], H. Yamamoto[1], A. Kawamura[1,7], N. Mizuno[1,7], T. Onishi[1,6], M. R. Morris[8], and Y. Fukui[1]

[1] Department of Physics, Nagoya University, Furo-cho, Chikusa-ku, Nagoya, Aichi 464-8602, Japan; enokiya@a.phys.nagoya-u.ac.jp
[2] Université de Nice Sophia-Antipolis, CNRS, Observatoire de Côte d'Azur, Laboratoire Lagrange, BP4229, F-06304 Nice Cedex 4, France
[3] Institut d'Astrophysique de Paris, CNRS, 98bis Bd Arago, F-75014 Paris, France
[4] Faculty of Science, Chiba University, Inage-ku, Chiba 263-8522, Japan
[5] Department of Astronomy and Earth Sciences, Tokyo Gakugei University, Koganei 594-1, Tokyo 184-8501, Japan
[6] Department of Astrophysics, Graduate School of Science, Osaka Prefecture University, 1-1Gakuen-cho, Nakaku, Sakai, Osaka 599-8531, Japan
[7] National Astronomical Observatory of Japan, Mitaka, Tokyo 181-8588, Japan
[8] Department of Physics and Astronomy, University of California, Los Angeles, CA 90095-1547, USA
Received 2012 May 24; accepted 2013 August 21; published 2013 December 13

ABSTRACT

We have discovered two molecular features at radial velocities of -35 km s^{-1} and 0 km s^{-1} toward the infrared Double Helix Nebula (DHN) in the Galactic center with NANTEN2. The two features show good spatial correspondence with the DHN. We have also found two elongated molecular ridges at these two velocities distributed vertically to the Galactic plane over 0°.8. The two ridges are linked by broad features in velocity and are likely connected physically with each other. The ratio between the ^{12}CO $J = 2$–1 and $J = 1$–0 transitions is 0.8 in the ridges which is larger than the average value 0.5 in the foreground gas, suggesting the two ridges are in the Galactic center. An examination of the K band extinction reveals a good coincidence with the CO 0 km s^{-1} ridge and is consistent with a distance of 8 ± 2 kpc. We discuss the possibility that the DHN was created by a magnetic phenomenon incorporating torsional Alfvén waves launched from the circum-nuclear disk and present a first estimate of the mass and energy involved in the DHN.

Key words: ISM: clouds – radio lines: ISM

1. INTRODUCTION

The Galactic center (GC) harbors a massive black hole, Sgr A*, and is still a most enigmatic region in the Galaxy after a few decades of observational studies at various wavelengths as well as theoretical studies. The highly complex distribution of various astronomical objects and the lack of optical images due to the heavy extinction make it difficult to disentangle the observed features into individual physical entities and to establish their interrelations (e.g., Morris & Serabyn 1996).

In spite of these difficulties, it is becoming increasingly evident that the magnetic field plays an important role in the GC region. Yusef-Zadeh et al. (1984) discovered the Radio Arc, in which synchrotron emission arises in highly ordered magnetic field lines vertical to the Galactic plane. Subsequently, more than 20 smaller non-thermal filaments were discovered to extend vertically to the Galactic plane within the central 300 pc of the GC (Morris & Yusef-Zadeh 1985; LaRosa et al. 2004; Yusef-Zadeh et al. 2004). Recently, based on molecular observations, Fukui et al. (2006) discovered two huge molecular loops within 5° of the GC and advocated that they are magnetic structures created by the Parker instability (Parker 1966). Follow-up studies have shown details of the physical properties of the molecular loops, including shock heating of the footpoints of the loops (Machida et al. 2009; Fujishita et al. 2009; Takahashi et al. 2009; Torii et al. 2010a, 2010b; Kudo et al. 2011). At infrared wavelengths, *Spitzer* images were used to identify the Double Helix Nebula (DHN), located 0°.6 to 0°.8 above Sgr A* (Morris et al. 2006). The DHN appears to have two intertwined helical strands reminiscent of deoxyribonucleic acid. Morris et al. (2006) proposed that the DHN is driven by torsional Alfvén waves that may be connected to the circumnuclear disk (CND) around Sgr A*. On the other hand, another possibility was discussed that the DHN may be associated with the eastern part of the GC lobe (Sofue & Handa 1984), which may be connected to the Radio Arc but not to Sgr A*, based on polarization measurements of 10 GHz and 5 GHz radio continuum radiation (Tsuboi & Handa 2010; Law et al. 2008). Most recently, the break in the non-thermal radio spectrum in the GC was used to infer a typical large-scale magnetic field of at least 50 μG within 200 pc of the GC (Crocker et al. 2010). These observational studies indicate that the magnetic field may play a crucial role in the gas kinematics in the GC.

Among these features, we shall here focus on the DHN. The previous study of the DHN is only at infrared wavelengths and the mass and energy involved in the DHN have not been estimated from observations. The basic physical properties of the DHN therefore remains elusive. In order to better understand its physical properties and possible connection with the relevant features, we have carried out a search for molecular counterpart(s) in the rotational transitions of CO toward the Central Molecular Zone (CMZ; Morris & Serabyn 1996) with the 4 m NANTEN2 telescope. The observations cover a large area of the CMZ with angular resolutions of 90″ and 180″, enabling us to make a direct comparison with the infrared distributions of the DHN. In this study we present discovery of possible molecular counterparts to the DHN and discuss their implications for the activity in the GC. A fuller account of these observations will be published separately (R. Enokiya et al. 2013, in preparation). The present paper is organized as follows. Section 2 describes the CO observations and Section 3 gives the results and an analysis of the near-infrared

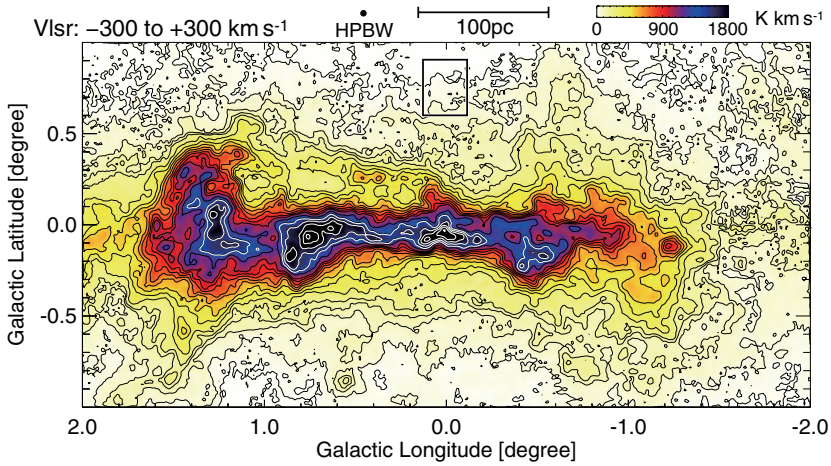

Figure 1. ^{12}CO $J = 2$–1 distribution integrated over the velocity range of −300 to +300 km s^{-1}. Contours are drawn at 15, 50, 100, 150, 200, 300, 400, 500, 600, 700, 800, 900, 1000, 1200, 1400, 1600, 1800, and 2000 K km s^{-1}. A box shows the displayed area of Figure 2.

(A color version of this figure is available in the online journal.)

extinction. Section 4 gives comparisons with other wavelengths and an overall discussion and Section 5 summarizes the paper.

2. OBSERVATIONS

Observations of the $J = 2$–1 transition of ^{12}CO at 230 GHz were made during the period from 2010 July to 2011 January with the NANTEN2 4 m submillimeter/millimeter telescope located at 4865 m above the sea level in Atacama, Chile. The total observing time was ∼250 hr. The half power beamwidth (HPBW) was 90″ as measured by observing Jupiter. The telescope was equipped with a 4 K cooled superconducting–insulator–superconducting (SIS) mixer receiver with a double sideband (DSB) system temperature, including the atmosphere toward the zenith, of ∼180 K. Spectroscopy was done with a digital spectrometer whose bandwidth and resolution were 1 GHz and 61 kHz, respectively. The velocity coverage and resolution were 1300 km s^{-1} and 0.08 km s^{-1}, respectively. Observations were made in the on-the-fly (OTF) mode and the final rms noise fluctuations are 0.35 K for a velocity resolution of 0.65 km s^{-1} after convolving the spectral data with a Gaussian function.

Deep observations of the $J = 1$–0 transition of ^{13}CO at 110 GHz toward $|l| < 0.^\circ25$ and $-0.^\circ5 < b < 1.^\circ0$ were carried out with NANTEN2 by using the OTF mode during 2011 April to June. A 4 K cooled SIS mixer receiver provided a typical system temperature of ∼270 K in DSB, and a digital spectrometer provided a bandwidth and resolution of 1 GHz and 61 kHz, which correspond to 2600 km s^{-1} and 0.17 km s^{-1}, respectively. We smoothed the obtained data to a velocity resolution of 0.51 km s^{-1} and angular resolution of 190″, and finally obtained rms noise fluctuations of ∼0.13 K for that velocity resolution.

Large-scale observations of the $J = 1$–0 transition of ^{12}CO and ^{13}CO emission toward $|l| < 10.^\circ0$ and $|b| < 1.^\circ0$ were carried out with NANTEN2 by using the OTF mode during a period from 2011 May to 2013 January. Typical system temperature including the atmosphere toward the zenith was 200–270 K in DSB, and a digital spectrometer provided a bandwidth and resolution of 1 GHz and 61 kHz. We smoothed the obtained data to an angular resolution of 200″, and finally obtained rms noise fluctuations of 0.5–1.0 K per channel for ^{12}CO and 0.30–0.35 K per channel for ^{13}CO. The velocities in the present paper always refer to the local standard of rest (LSR).

3. RESULTS

3.1. Discovery of Candidate Molecular Counterparts to the DHN

Figure 1 shows the integrated intensity distributions of ^{12}CO $J = 2$–1 emission in an area of 4° in l by 2° in b centered at $(l, b) = (0.^\circ0, 0.^\circ0)$ obtained with NANTEN2. The main components of the CMZ are distributed at $|b| < 0.^\circ5$. The position of the DHN is shown by a box toward $(l, b) = (0.^\circ0, 0.^\circ75)$ in this figure. We show the velocity channel distributions of the ^{12}CO $J = 2$–1 emission from the full region in Figures 15–17. By analyzing the velocity structure in these figures, we have found two possible molecular counterparts to the DHN at two different velocities.

Figures 2(a) and (b) show the candidate counterparts of the DHN at velocity near −35 km s^{-1} and 0 km s^{-1}, respectively (hereafter, the −35 km s^{-1} and 0 km s^{-1} features, respectively). These two linear features are both aligned with the DHN, and extend up to $b = 0.^\circ86$ (the −35 km s^{-1} feature) and $b = 0.^\circ83$ (the 0 km s^{-1} feature). The −35 km s^{-1} feature abuts the DHN on its western side, while the 0 km s^{-1} feature is centered along the eastern edge of the DHN. Both have widths of 10–20 pc, if they are located at the distance of the GC, 8 kpc. We also made observations toward these two CO features with higher spatial resolutions of ∼33″, by using the CSO 10 m and Mopra 22 m telescopes in the CO $J = 2$–1 and $J = 1$–0 transitions, and found that the 0 km s^{-1} feature apparently coincides with the DHN and that the −35 km s^{-1} feature is spatially anti-correlated with the DHN. These results reinforce the association of the two CO features with the DHN and will be presented separately (Torii et al. 2013).

Figures 3(a) and (b) show the detailed velocity distributions of the two features and indicate that they have similar velocity gradients of $\sim 0.^\circ4$ km s^{-1} pc^{-1} in the east–west direction in the same sense. We estimate the molecular masses of the −35 km s^{-1} ($0.^\circ6 \leqslant b \leqslant 0.^\circ86$) and 0 km s^{-1} features ($0.^\circ6 \leqslant b \leqslant 0.^\circ83$) to be 4×10^3 $M_\odot$ and 1×10^4 $M_\odot$, respectively, for an assumed X factor of 0.7×10^{20} cm^{-2}/(K km s^{-1}) (Torii et al. 2010b) at 8 kpc.

3.2. Molecular Ridges Rising from the Galactic Plane

We have found two other CO components apparently connected to the CO-emitting candidate DHN counterparts and we describe their distribution in this subsection.

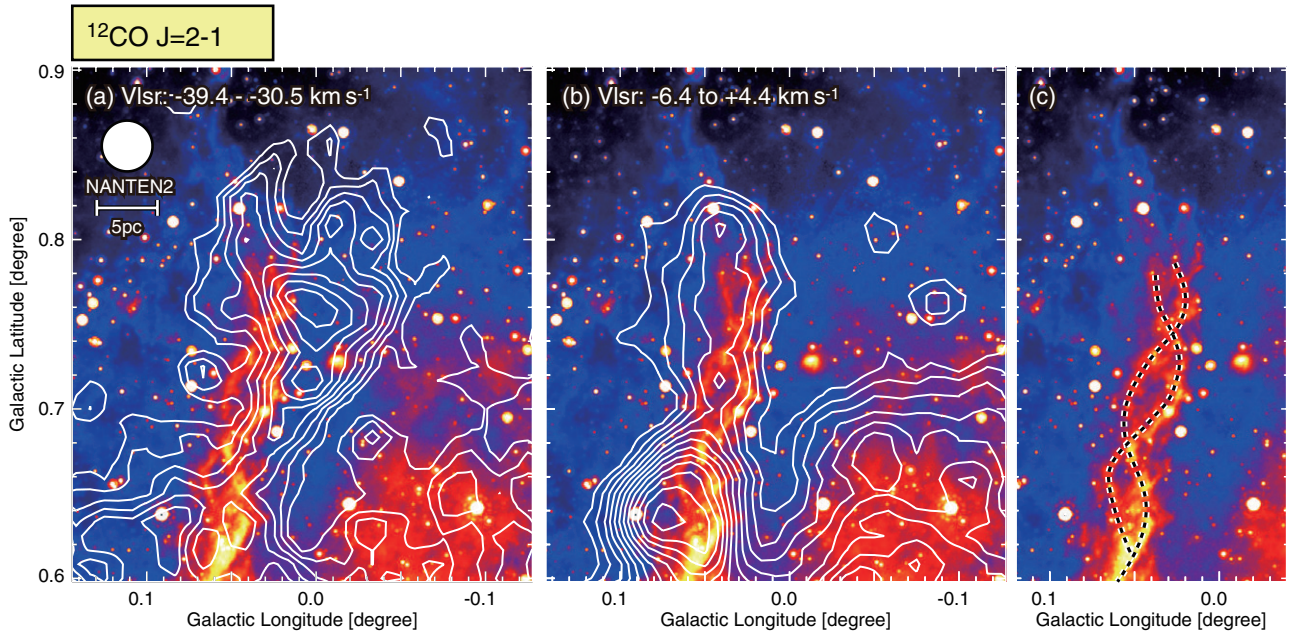

Figure 2. (a) and (b) ^{12}CO $J = 2$–1 integrated intensity distributions of the two CO counterparts of the DHN superposed on the *Spitzer* 24 μm image. (a) -35 km s^{-1} feature. Contours are plotted at every 0.7 K km s^{-1} from 1.0 K km s^{-1}. (b) 0 km s^{-1} feature. Contours are plotted at every 1.4 K km s^{-1} from 10 K km s^{-1}. (c) The *Spitzer* 24 μm image with schematic lines of the two helical patterns.

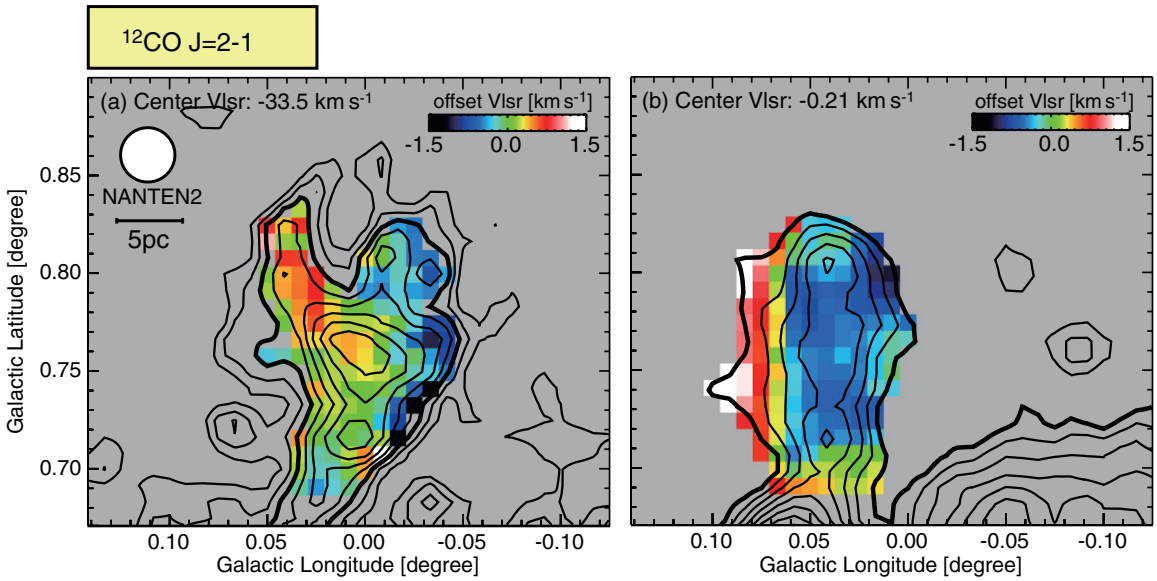

Figure 3. Distributions of the intensity-weighted averaged velocity of the -35 km s^{-1} and 0 km s^{-1} features. The images show velocity offsets from their central velocities, -33.5 km s^{-1} and -0.21 km s^{-1}. Contours shows the integrated ^{12}CO $J = 2$–1 emission and are plotted at the same levels as in Figures 2(a) and (b).

Figure 4 shows the large-scale ^{12}CO $J = 2$–1 distribution, including the two DHN counterpart features located in the small box. In Figure 4(a), we find that there is a ridge-like CO feature in the large box (hereafter, the -35 km s^{-1} ridge) just below the -35 km s^{-1} feature, extending toward the Galactic plane (at $l = -0.^\circ1$–$0.^\circ2$). The -35 km s^{-1} ridge cannot be distinguished at latitudes $< 0.^\circ2$ because of confusion with the extended emission along the Galactic plane. Most of the ^{12}CO emission in Figure 4(a) is from the CMZ, since the distribution is similar to that of the main body of the CMZ (Figure 1). In Figure 4(b) the 0 km s^{-1} feature is clearly seen in the small box. In Figure 4(b) we find a narrow ridge component (at $l = 0.^\circ0$–$0.^\circ2$) at latitudes below $\sim 0.^\circ6$ (hereafter, the 0 km s^{-1} ridge), vertically extending down to $b \sim 0.^\circ2$ (in the large box). It is located just below the 0 km s^{-1} feature and has a width a few times larger than that of the 0 km s^{-1} feature. This ridge is affected by self-absorption by foreground gas below $b = 0.^\circ2$, while the optically thin ^{13}CO $J = 1$–0 emission (Figure 5(b)) shows that the 0 km s^{-1} ridge extends to $b = 0.^\circ0$. Some of the ^{12}CO features evident at higher Galactic latitudes in Figure 4(b), e.g., those at $(l, b) = (-1.^\circ7$ to $-0.^\circ9$, $-1.^\circ0$ to $-0.^\circ2)$, $(-1.^\circ0$ to $-0.^\circ6$, $-1.^\circ0$ to $-0.^\circ5)$ and $(0.^\circ4$ to $0.^\circ9$, $0.^\circ5$ to $0.^\circ8)$, are foreground features outside the GC, while the main CO emission in the region $(l, b) = (-1.^\circ2$ to $+1.^\circ8$, $-0.^\circ5$ to $+0.^\circ4)$ is mostly from the CMZ. The ^{12}CO feature at $(l, b) = (0.3, 0.5$ to $0.7)$ having velocity around -35 km s^{-1} may possibly be associated with

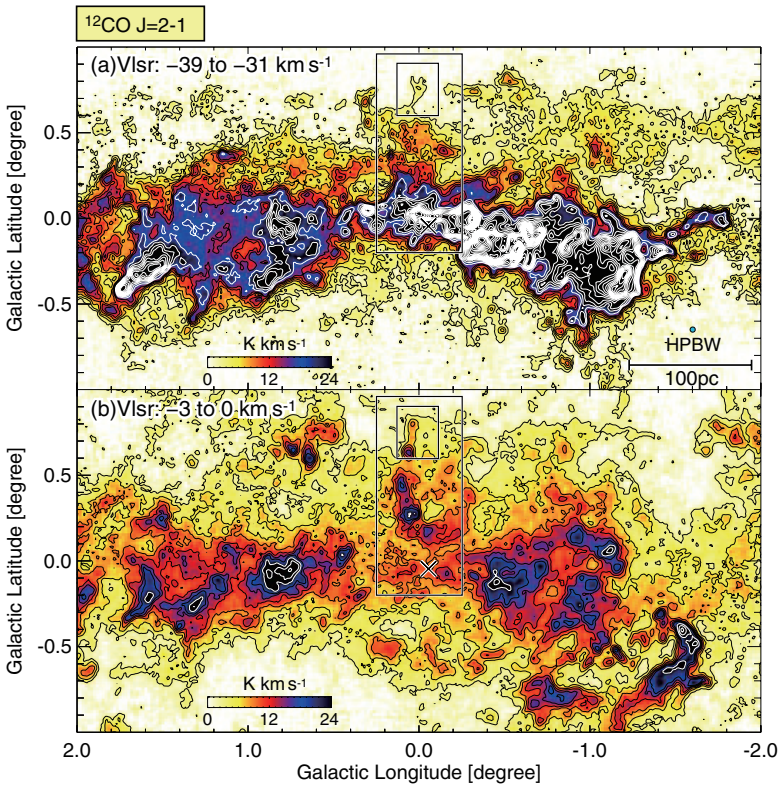

Figure 4. Integrated intensity distributions of ^{12}CO $J = 2$–1 emission toward $(l, b) = (-2\overset{\circ}{.}0$ to $+2\overset{\circ}{.}0, -1\overset{\circ}{.}0$ to $+1\overset{\circ}{.}0)$. A cross indicates the position of SgrA*, and big boxes and small boxes show the displayed regions of Figures 2 and 5, respectively. (a) Map of the -35 km s^{-1} feature integrated over the velocity range from -31 to -39 km s^{-1}. Contours are drawn every 3 K km s^{-1} from 3 K km s^{-1} (black lines) and every 6 K km s^{-1} from 24 K km s^{-1} (white lines). (b) Map of the 0 km s^{-1} feature integrated over the velocity range from -3 to 0 km s^{-1}. Contours are drawn every 3 K km s^{-1} from 3 K km s^{-1} and every 6 K km s^{-1} from 24 K km s^{-1}.

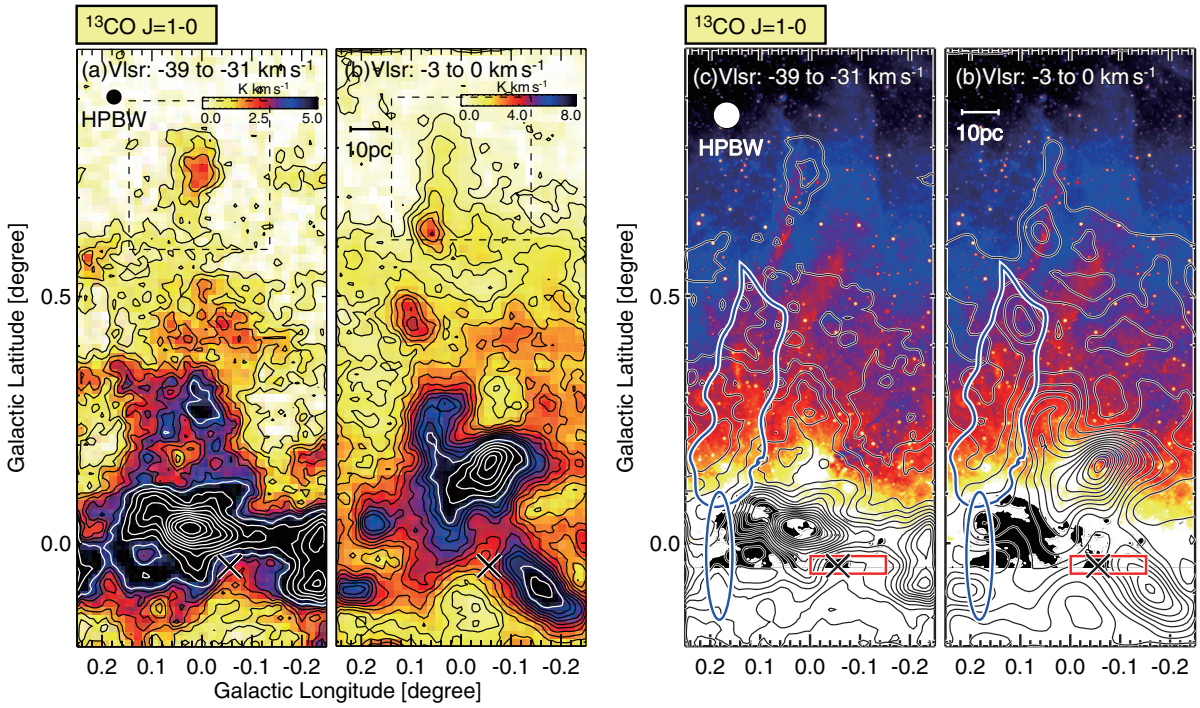

Figure 5. (a) and (b) Integrated intensity distributions of the ^{13}CO $J = 1$–0 emission toward $(l, b) = (-0\overset{\circ}{.}25$ to $+0\overset{\circ}{.}25, -0\overset{\circ}{.}2$ to $+1\overset{\circ}{.}0)$. Crosses depict the location of SgrA*. (a) Map of the -35 km s^{-1} feature integrated over the velocity range from -31 to -39 km s^{-1}. Contours are drawn every 0.6 K km s^{-1} from 0.6 K km s^{-1} and then every 1.5 K km s^{-1} from 4.2 K km s^{-1}. (b) Map of the 0 km s^{-1} feature integrated over the velocity range from -3 to 0 km s^{-1}. Contours are drawn every 0.6 K km s^{-1} from 0.6 K km s^{-1} and then every 1.2 K km s^{-1} from 7.2 K km s^{-1}. (c) and (d) Superpositions of smoothed contours of ^{13}CO $J = 1$–0 and the *Spitzer* 24 μm image. Red box and blue ellipse give the approximate extent of the Radio Arc and CND, respectively. Blue contour is 50 mJy beam^{-1} of linearly polarized intensity at 10 GHz, showing the approximate extent of the polarized plume. (c) -35 km s^{-1} feature and ridge. Contours are plotted at every 1.5 K km s^{-1} from 1.5 K km s^{-1}. (d) 0 km s^{-1} feature and ridge. Contours are plotted at every 0.8 K km s^{-1} from 1.2 K km s^{-1}.

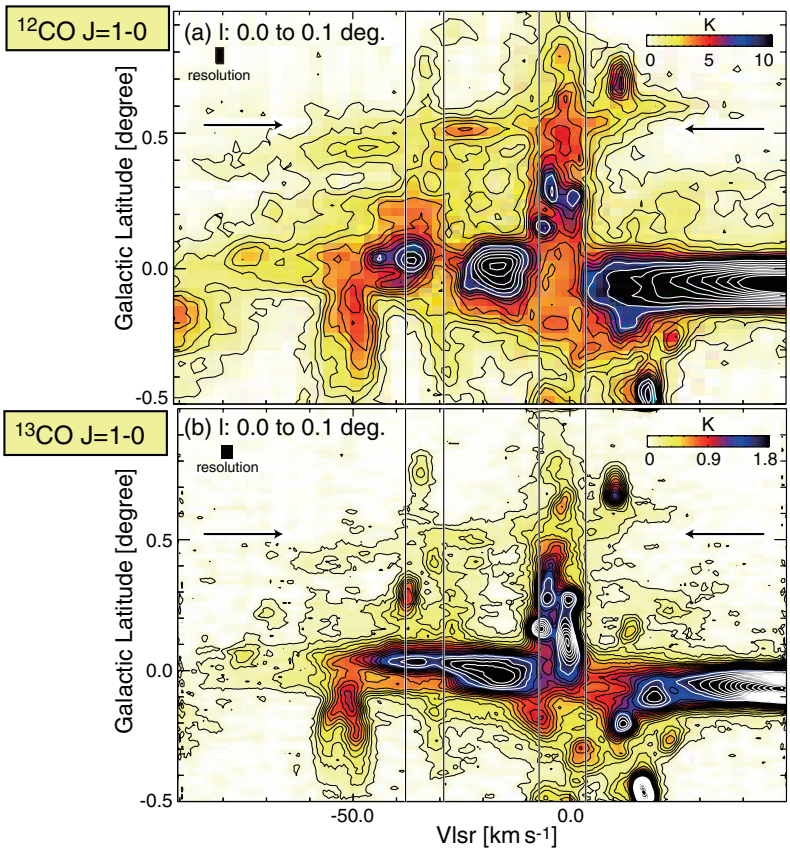

Figure 6. Position–velocity distributions of averaged CO intensities toward the -35 km s^{-1} and 0 km s^{-1} ridges. The integration range in galactic longitude is 0.°0 to +0.°1. (a) ^{12}CO $J = 1$–0. Contours are plotted at every 0.7 K from 0.5 K (black) and every 2.0 K from 7.5 K (white). Vertical lines delineate the two ridges, and arrows indicate the broad feature connecting the two ridges. (b) ^{13}CO $J = 1$–0. Contours are plotted at every 0.10 K from 0.08 K (black) and then every 0.2 K from 1.48 K (white). (A color version of this figure is available in the online journal.)

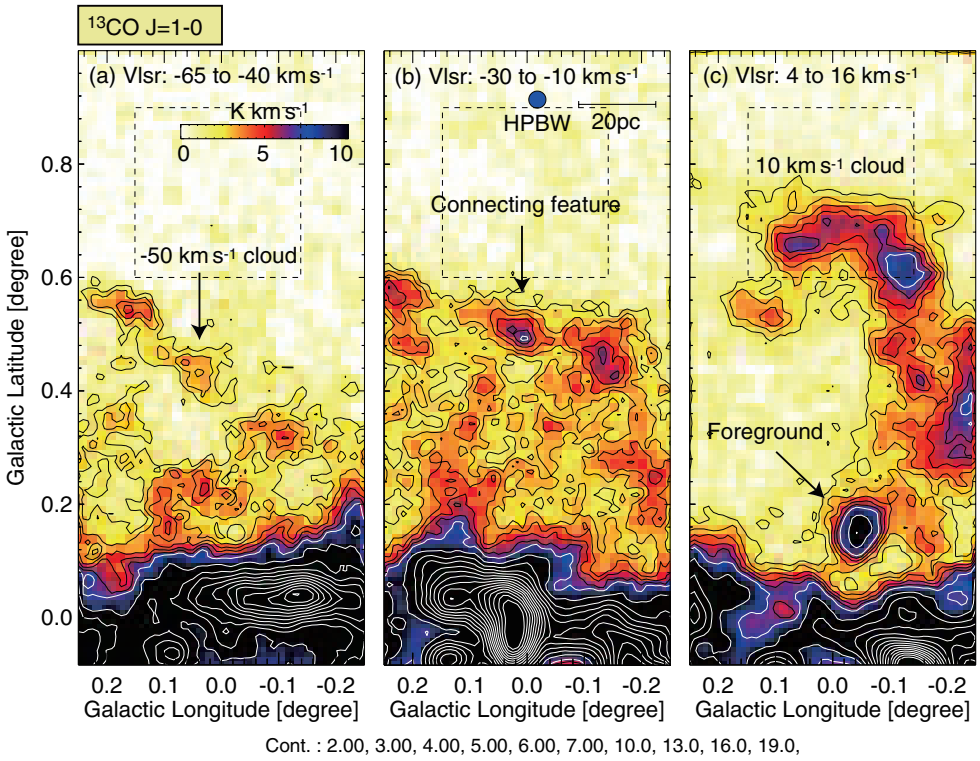

Figure 7. Integrated intensity maps of ^{13}CO $J = 1$–0 emission in different velocity ranges. Contour values and integrated velocity ranges for each map are shown at the bottom and top of each figure, respectively. Dashed boxes show the same region of Figure 2, where the DHN is distributed. (A color version of this figure is available in the online journal.)

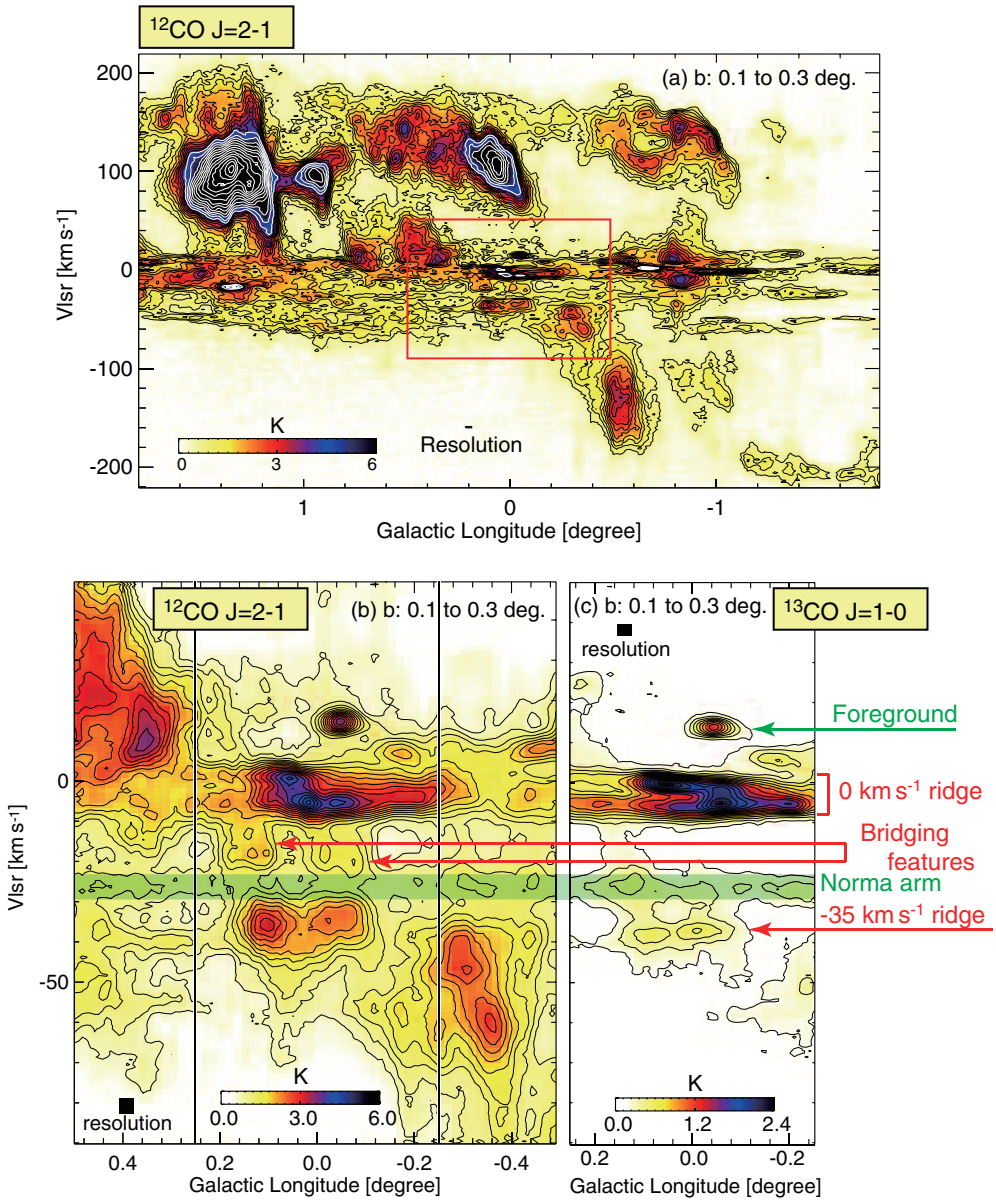

Figure 8. Position–velocity distributions of averaged CO intensities toward the -35 km s^{-1} and 0 km s^{-1} ridges in the latitude range $0.^\circ1 \leqslant b \leqslant 0.^\circ3$. (a) Large-scale longitude–velocity diagram of ^{12}CO $J = 2$–1. (b) Close up view of the red box in panel (a). Contours are plotted at every 0.25 K from 0.75 K. Vertical lines show the region shown in panel (c). (c) ^{13}CO $J = 1$–0. Contours are plotted at every 0.15 K from 0.2 K.

the -35 km s^{-1} ridge, although no significant enhancement in the ^{12}CO 2–1/1–0 intensity ratio of the feature (Figure 10(a)) does not strongly support the association.

Figures 5(a) and (b) show the ^{13}CO $J = 1$–0 emission toward the two ridges. In Figure 5(a) the -35 km s^{-1} ridge has a peak in the Galactic plane at $l = 0.^\circ0$, whereas its distribution below $b = 0.^\circ1$ is not clear due to contamination with the CMZ. Above $b = 0.^\circ15$, the -35 km s^{-1} ridge has two features in $l = -0.^\circ1$ to $0.^\circ0$ and in $l = 0.^\circ05$ to $0.^\circ15$ at $b = 0.^\circ2$ that apparently merge at $(l, b) = (0.^\circ0, 0.^\circ3)$. Beyond $0.^\circ35$ we see continuation of ^{13}CO up to $0.^\circ55$. The 0 km s^{-1} ridge is seen in Figure 5(b). The strong peak toward $(l, b) = (-0.^\circ05, 0.^\circ20)$ is foreground, as shown by the near infrared extinction (see Figures 11(a) and (d)). Except for this feature we see the ridge at $b = -0.^\circ1$ to $0.^\circ3$ and an additional peak at $b = 0.^\circ45$. Figures 5(c) and (d) show a comparison with the *Spitzer* infrared image. We note that the CO ridges show spatial correspondence with the infrared distribution in $l = -2.^\circ0$ to $2.^\circ0$ and b above $0.^\circ3$, where contamination is not so heavy. In particular, the correspondence is good for the infrared DHN and its filament directed toward the Galactic plane (Figure 5). We estimate the molecular masses of the -35 km s^{-1} and the 0 km s^{-1} ridges to be 2×10^5 $M_\odot$ and 1×10^5 $M_\odot$, respectively, for an assumed X factor 0.7×10^{20} cm^{-2}/(K km s^{-1}) (Torii et al. 2010b) at 8 kpc. Detailed spatial distributions of these ridges are shown in Figures 18 and 19.

3.3. Velocity Distribution of the CO Ridges

Figures 6(a) and (b) show the velocity–latitude distributions of the ^{12}CO $J = 1$–0 and ^{13}CO $J = 1$–0, respectively, where the integration range in galactic longitude is from $0.^\circ0$ to $0.^\circ1$. The two CO ridges appear as narrow features with a FWHM line width of 5–10 km s^{-1}. The -35 km s^{-1} ridge appears at $b = 0.^\circ2$–$0.^\circ35$ with a velocity span of $\lesssim$20 km s^{-1} and the 0 km s^{-1} ridge at $b = 0.^\circ2$–$0.^\circ6$ with a velocity span of 15 km s^{-1}. In Figure 6(a) we find significant self-absorption features at velocities of 0 km s^{-1}, -30 km s^{-1} and -50 km s^{-1}

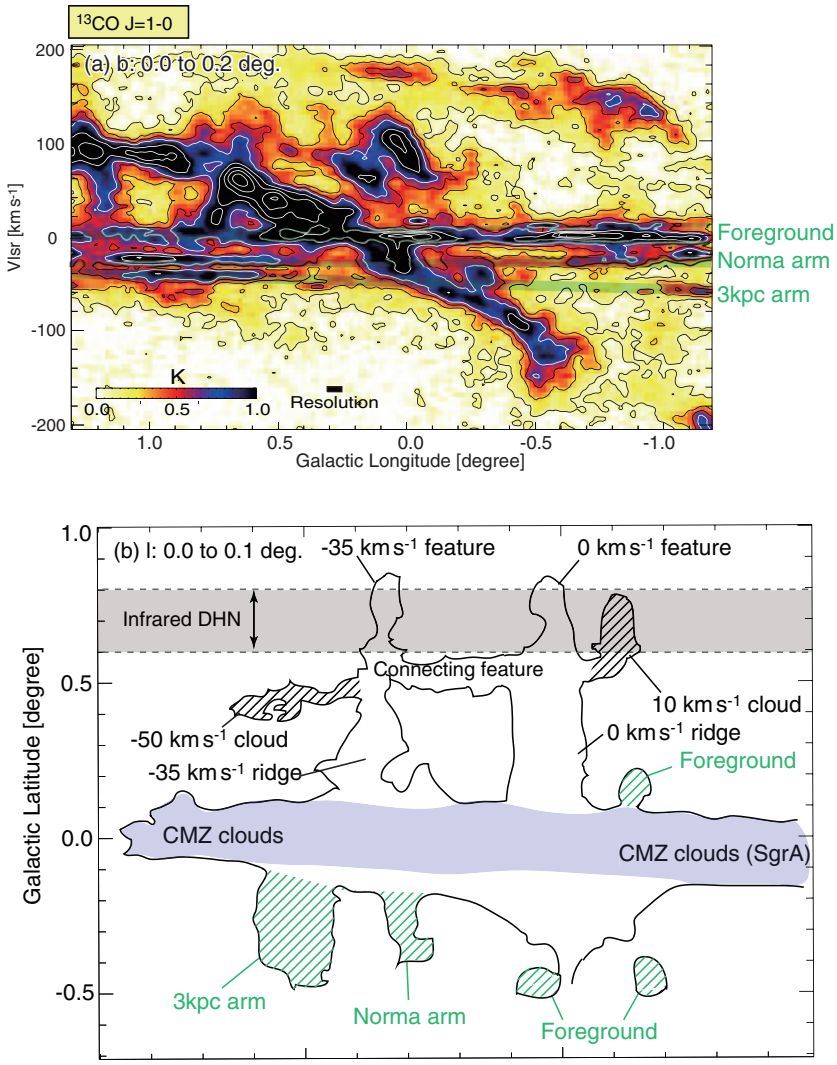

Figure 9. (a) Longitude–velocity diagrams of ^{13}CO $J = 1$–0 integrated from $-0\overset{\circ}{.}03$ to $+0\overset{\circ}{.}20$. Green lines show emission from foreground clouds. (b) Schematic image of Figure 6(b). Green hatching and gray belt mean foreground cloud and dense molecular gas located in the CMZ, respectively.

at $|b| \lesssim 0\overset{\circ}{.}2$, while they are not seen in the optically thin ^{13}CO in Figure 6(b). The self-absorption is attributable to the foreground low-excitation gas. The 0 km s^{-1} CO ridge extends to the Galactic plane at $b = 0\overset{\circ}{.}0$. The strongest broad feature seen at b less than $0\overset{\circ}{.}2$ is the CMZ. There is another broad feature which appears to be connecting the -35 km s^{-1} and 0 km s^{-1} ridges at $b = 0\overset{\circ}{.}5$, as indicated by black arrows in Figure 6 (see also Figures 7(b) and 9(b)). There is also weak emission from 35 km s^{-1} to 0 km s^{-1} filling the region below $b = 0\overset{\circ}{.}5$ between the two CO ridges.

We present more details of the connecting feature between the two ridges in Figure 7, which shows the integrated intensity distributions of the ^{13}CO $J = 1$–0 emission in three different velocity ranges; (a) the -50 km s^{-1} cloud in a velocity range of -65 km s^{-1} to -40 km s^{-1}, (b) the connecting feature in a velocity range of -30 km s^{-1} to -10 km s^{-1}, and (c) the 10 km s^{-1} cloud in a velocity range of 4 km s^{-1} to 16 km s^{-1}. In Figure 7(b), the peak located at $(l, b) = (0\overset{\circ}{.}0, 0\overset{\circ}{.}5)$ is that of the connecting feature and other two peaks at $(l, b) = (-0\overset{\circ}{.}12, 0\overset{\circ}{.}45)$ and $(0\overset{\circ}{.}25, 0\overset{\circ}{.}55)$ are also possibly related to the connecting feature (see Figure 16). The -50 km s^{-1} cloud is extended from $(l, b) = (-0\overset{\circ}{.}1, 0\overset{\circ}{.}3)$ to $(0\overset{\circ}{.}14, 0\overset{\circ}{.}55)$ with a tilt of 40° to the Galactic plane and the 10 km s^{-1} cloud shows a arced shape elongated in l at $b = 0\overset{\circ}{.}7$ with extension toward the Galactic plane at $l = -0\overset{\circ}{.}1$. The connecting feature seems to be unrelated to the -50 km s^{-1} (a) and 10 km s^{-1} clouds (c), since the three show significantly different spatial distributions.

The CO distribution toward the two CO ridges is complicated due to heavy contamination and self-absorption by different features in the line of sight, especially near $V_{\rm lsr} = 0$ km s^{-1}. It is not straightforward to disentangle the contamination by using only the two-dimensional distribution. Figure 8(a) shows a large-scale longitude–velocity diagram of ^{12}CO $J = 2$–1 emission integrated between $b = 0\overset{\circ}{.}1$ to $0\overset{\circ}{.}3$. The continuous CO feature which is distributed from $(l, v) = (-0\overset{\circ}{.}6, -150$ km s$^{-1})$ to $(0\overset{\circ}{.}2, 30$ km s$^{-1})$ is ascribed to part of the CMZ, because the velocity range is similar to that of the CMZ (Sofue 1995; Tsuboi 1999; Molinari et al. 2011). Figures 8(b) and (c) show close-up views of the red box in Figure 8(a) in ^{12}CO $J = 2$–1 and ^{13}CO $J = 1$–0. Figure 8(b) shows that the -35 km s^{-1} CO ridge continues as two bridging features at $l = -0\overset{\circ}{.}05$ and $0\overset{\circ}{.}1$ to the CO ridge at 0 km s^{-1}, while it shows an intensity depression at -30 km s^{-1} due to the line absorption by the Norma arm. This distribution supports the hypothesis that the two ridges

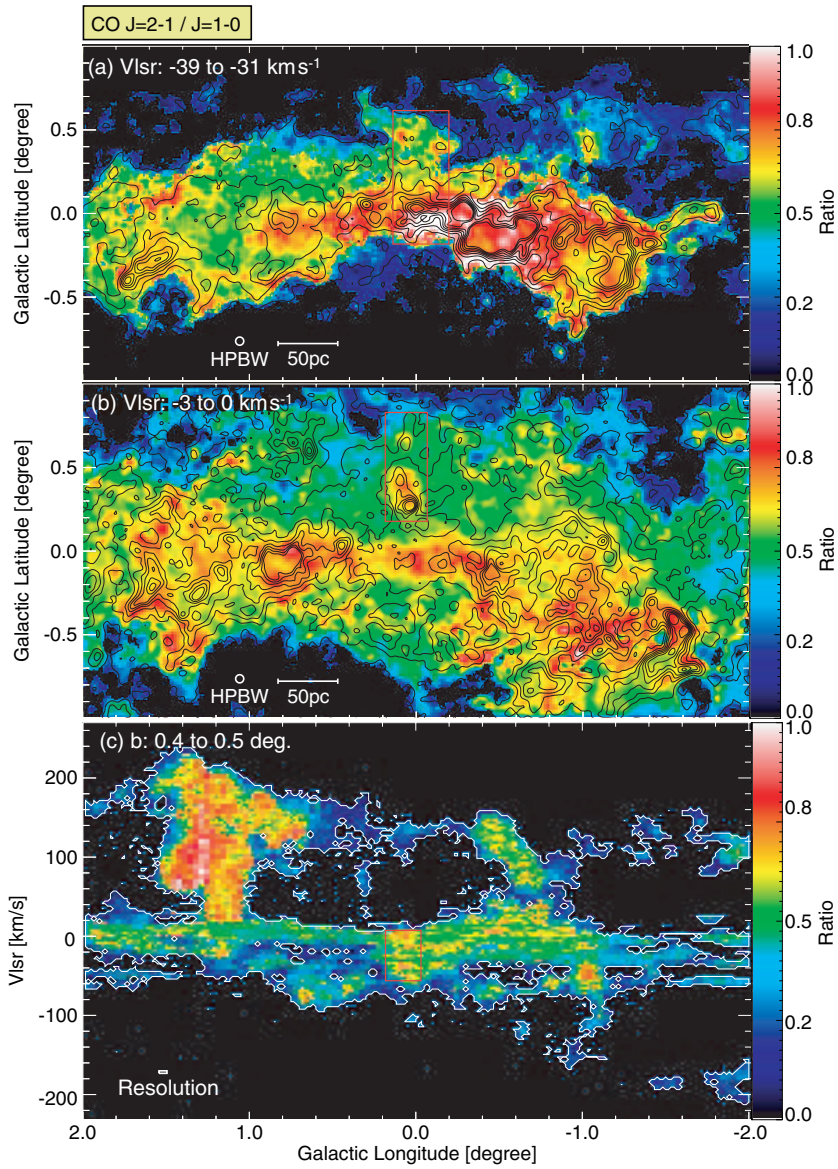

Figure 10. (a) and (b) Intensity ratio distributions between ^{12}CO $J = 2$–1 and ^{12}CO $J = 1$–0 overlaid with ^{12}CO $J = 2$–1 contours. The integration range in $V_{\rm lsr}$ is shown in the figure. Contours are plotted at every 2 K from 2 K. (c) Longitude–velocity diagram of CO ridges. Color shows ratio distributions between ^{12}CO $J = 2$–1 and ^{12}CO $J = 1$–0 overlaid with ^{12}CO $J = 2$–1 contours. The integration range in b is shown in the figure. Red boxes show the region around the two CO ridges, which has a relatively higher line intensity ratio.

are connected by the two bridging features, and that the $l = 0\overset{\circ}{.}1$ bridging feature, which has a ^{13}CO counterpart, seems to extend further to -70 km s^{-1} in Figure 8(b). We note that the ^{12}CO emission at -40 km s^{-1} in Figure 8(b) is the 3 kpc arm outside the GC and is unrelated with the CO ridges. Detailed velocity distributions of the ^{12}CO $J = 2$–1 and ^{13}CO $J = 1$–0 emission are presented in Figures 20 and 21.

In order to have a comprehensive view of the complicated features presented above, Figure 9(a) shows a longitude–velocity diagram toward the CO ridges in ^{13}CO $J = 1$–0. The foreground features have narrow linewidths and are more extended in the sky than those in the GC and are indicated by the green lines at +10 km s^{-1}, 0 km s^{-1}, -30 km s^{-1}and -50 km s^{-1} in Figure 9(a). Figure 9(b) shows a schematic diagram of Figure 6(b). The foreground features in Figure 9(a) are indicated by the green color. This figure shows that the -35 km s^{-1} ridge appears to be connected with the 0 km s^{-1} feature at $b = 0\overset{\circ}{.}5$, while the two bridging features are too faint to be seen here. The -50 km s^{-1} cloud and the 10 km s^{-1} cloud shown by black hatching may be foreground features, but their line-of-sight locations are not certain from the present results alone.

3.4. Excitation Conditions in the 0 km s^{-1} Feature and the Two CO Ridges

The molecular gas in the GC generally shows higher-excitation states reflecting higher temperature than that in the Galactic disk (e.g., Morris & Serabyn 1996; Torii et al. 2010a; Kudo et al. 2011). The excitation state of the gas can therefore be used as a determinant of whether the CO features are likely in the GC. In the CMZ, Sawada et al. (1999) found that the average value for the ^{12}CO $J = 2$–1/1–0 intensity ratio is 0.96 ± 0.01, where their ^{12}CO data were sampled at 7.5 arcmin intervals with 9 arcmin HPBW for $l = \pm 3\overset{\circ}{.}0$, $b = \pm 1\overset{\circ}{.}0$,

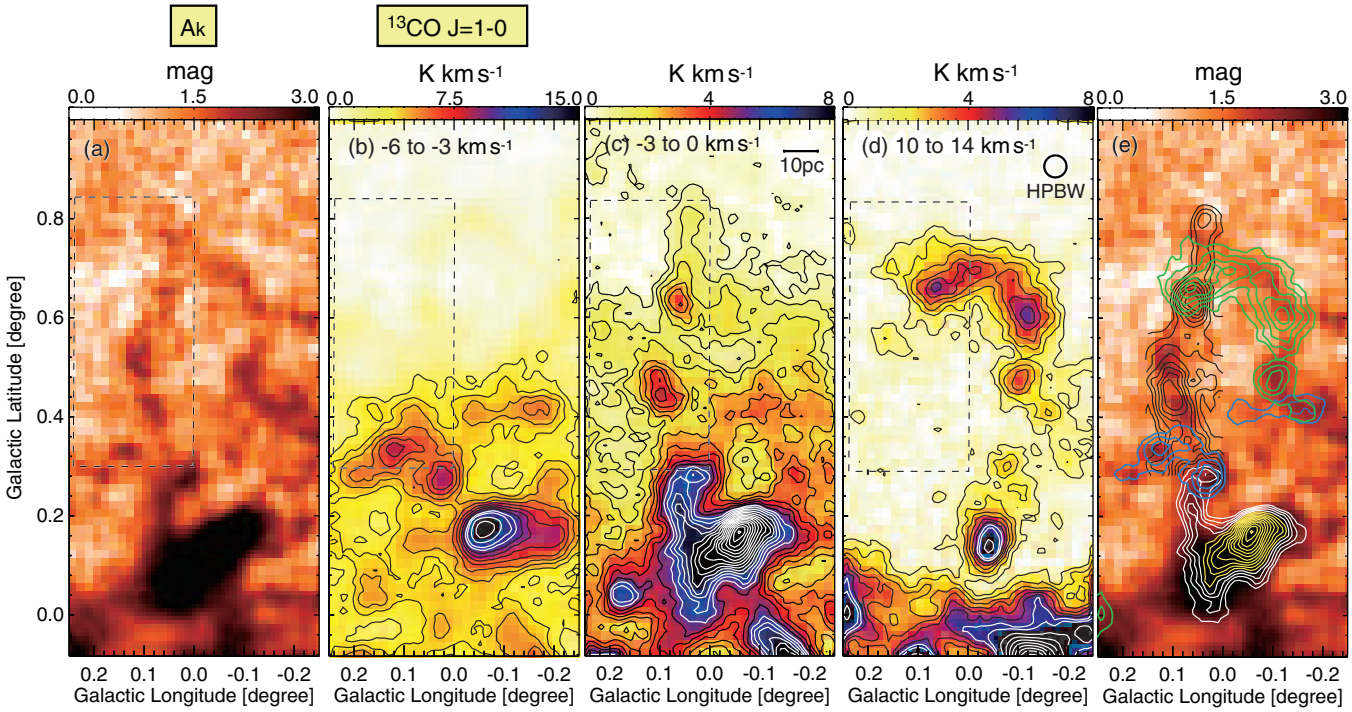

Figure 11. (a) A 2MASS A_K extinction map toward the DHN. (b) ^{13}CO $J = 1$–0 distributions integrated from -6 to -3 km s^{-1}. Contours are plotted every 2 K km s^{-1} from 4 K km s^{-1} and then every 4 K km s^{-1} from 34 K km s^{-1}. (c) ^{13}CO $J = 1$–0 distributions of the 0 km s^{-1} ridge and feature. Contours are plotted every 0.6 K km s^{-1} from 0.6 K km s^{-1}. (d) ^{13}CO $J = 1$–0 distributions of the 10 km s^{-1} cloud. Contours are plotted every 0.8 K km s^{-1} from 1.0 K km s^{-1}. The dashed boxes show the field used for the simulation of the stellar extinction. (e) The same figure as (a) with CO contours in various velocity ranges related to dark filaments in the figure.

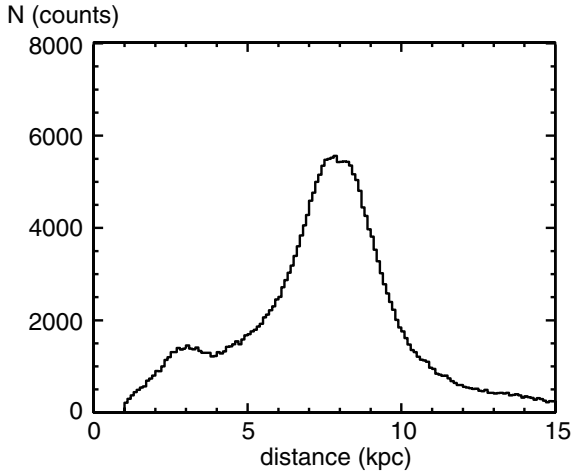

Figure 12. Distance plot toward a given field depicted by boxes in Figure 11. The vertical axis shows the number of simulated stars.

at a velocity resolution of 2 km s^{-1} over a velocity span of $\pm$300 km s^{-1}. The ratio is, however, sensitive to the velocity resolution and spatial sampling rate employed. By using the NANTEN2 OTF data with full sampling on a 1 arcmin grid with 2.6 arcmin HPBW, we find that the ^{12}CO $J = 2$–1/1–0 ratio, $R_{2-1/1-0}$, is >0.7 in the CMZ, reaching more than 1 in some positions, 0.5–0.6 in the largest velocity features in the "parallelogram" in the l–v diagram toward the CMZ (e.g., Binney et al. 1991). Part of the foreground gas, e.g., the CO gas at (l, b, v) = (0.2–1.0, 0.5–0.7, -10 to +10), shows low line ratio like 0.4–0.5, whereas some of the foreground gas toward the *Spitzer* 8 μm features (Figure 22) shows enhanced ratio like 0.8 as seen in the ^{12}CO feature at (l, b, v) = (-1.7 to -1.2, -0.8 to -0.2, -5.1 to +2.5). These full results of $R_{2-1/1-0}$ toward the CMZ region will be published separately (K. Torii et al. 2013, in preparation).

Figure 10 shows $R_{2-1/1-0}$ over the whole region of the present study, including the DHN. Figure 10(a) shows that the -35 km s^{-1} ridge at (l, b) = ($-0\overset{\circ}{.}2$ to $+0\overset{\circ}{.}1$, $0\overset{\circ}{.}4$ to $0\overset{\circ}{.}5$) shows a high line intensity ratio above 0.7 and is conspicuous in the region above $b = 0\overset{\circ}{.}2$. The figure also shows that regions of a high ratio are seen toward the CMZ and the other local *Spitzer* features having an associated heat source (Figure 22). It is possible that the ratio is affected by self-absorption in (l, b, v) = ($-0\overset{\circ}{.}5$ to $+0\overset{\circ}{.}5$, $-0\overset{\circ}{.}2$ to $+0\overset{\circ}{.}2$, -20 km s^{-1} to 20 km s^{-1}) in Figures 10(a) and (b). Finally, Figure 10(c) shows a longitude–velocity diagram of the ratio and that the two CO ridges as well as the bridging features show an enhanced ratio above 0.7, which is different from the other foreground features showing a smaller ratio around 0.3 - 0.5. Accordingly, we suggest that the $R_{2-1/1-0}$ enhancements in the CO ridges favor their location in the GC.

3.5. Distance Estimation by an Analysis of the Near-infrared Stellar Extinction

In order to make an independent estimate of the distance of the CO features and ridges, we have examined the distribution of near-infrared extinction derived from 2MASS data (Dobashi 2011) and have made a comparison with CO distributions.

Figure 11(a) shows the distribution of A_K extinction toward the CO features and ridges. We see significant extinction toward the 0 km s^{-1} ridge in addition to several additional features. We identify each feature by comparing it with the CO distribution. Figures 11(b)–(d) show the ^{13}CO $J = 1$–0 integrated intensity distributions for three velocity ranges of -6 km s^{-1} to -3 km s^{-1}, -3 km s^{-1} to 0 km s^{-1}, and 10 to 14 km s^{-1}, respectively. We find that the 0 km s^{-1} feature

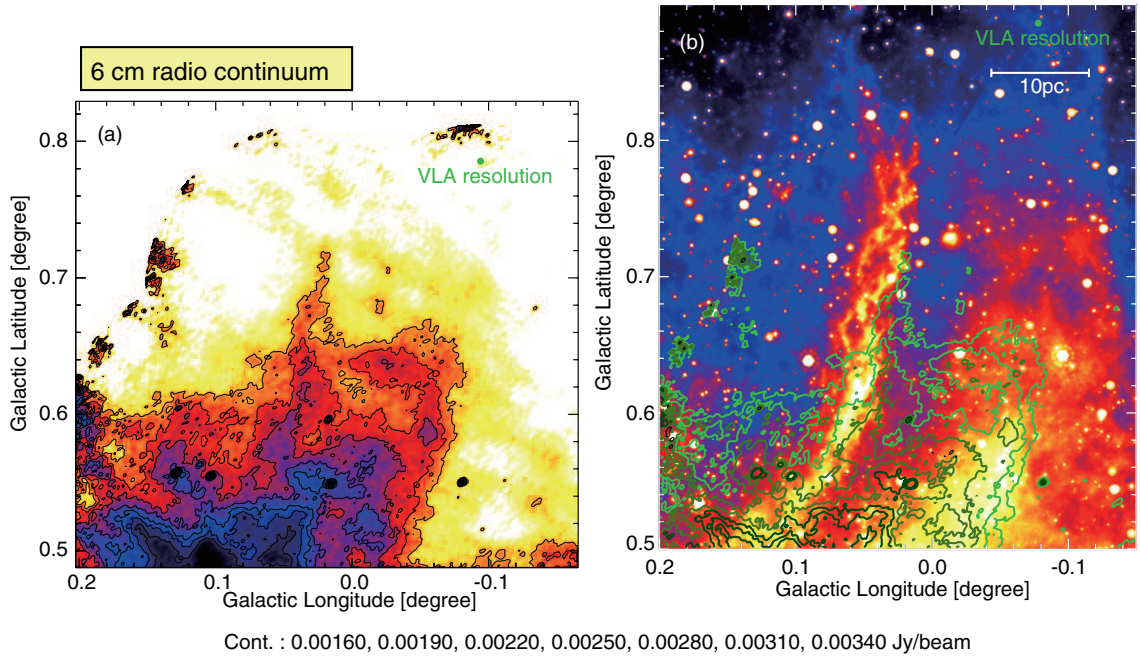

Figure 13. (a) 6 cm radio continuum distribution given by Law et al. (2008). (b) Contours of (a) superposed on the *Spitzer* 24 μm image. (A color version of this figure is available in the online journal.)

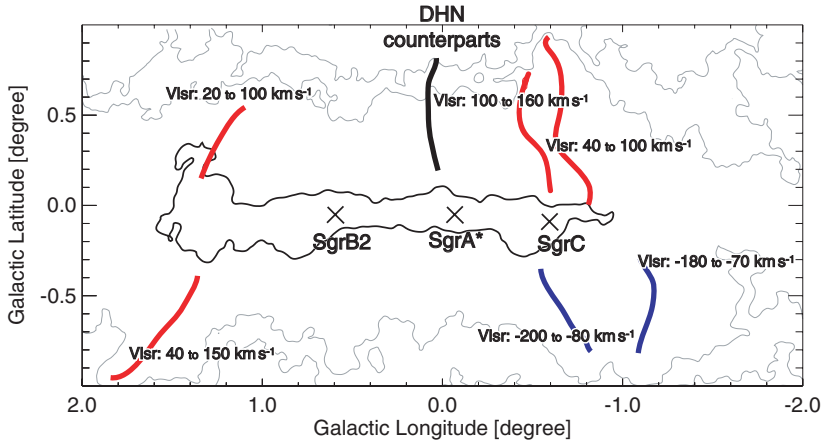

Figure 14. Schematic image of filament-like molecular features. Black contour shows the main molecular complex of the CMZ. Gray contours show diffuse high-latitude gases first detected by our observation. Each molecular filament feature can be seen in the detailed large-scale velocity channel maps of Figures 15–17. (A color version of this figure is available in the online journal.)

(Figure 11(c)) shows a good correspondence with the dark filament at $(l, b) = (0\overset{\circ}{.}00$ to $0\overset{\circ}{.}25$, $0\overset{\circ}{.}3$ to $0\overset{\circ}{.}85)$ enclosed by dashed lines in Figure 11(a). The other filamentary features have counterparts in Figures 11(b)–(d); the extinction feature at $(l, b) = (0\overset{\circ}{.}1, 0\overset{\circ}{.}3)$ corresponds to ^{13}CO emission between -6 km s^{-1} to -3 km s^{-1}, those in $(l, b) = (-0\overset{\circ}{.}15$ to $0\overset{\circ}{.}1$, $+0\overset{\circ}{.}1$ to $0\overset{\circ}{.}3)$ and $(-0\overset{\circ}{.}1$ to $+0\overset{\circ}{.}1$, $0\overset{\circ}{.}0$ to $0\overset{\circ}{.}2)$ to the ^{13}CO in -3 km s^{-1} to 0 km s^{-1}, and that at $(l, b) = (0\overset{\circ}{.}25, 0\overset{\circ}{.}0)$ to the ^{13}CO in 10 km s^{-1} to 14 km s^{-1}, as shown by an overlay with the extinction in Figure 11(e).

In order to estimate the distance to the 0 km s^{-1} feature, which shows good coincidence with the stellar extinction, we used the stellar population synthesis model, the Besanćon Galaxy Model, by Robin et al. (2012). This model includes a bar and a thick bulge adopted from the three-dimensional extinction model (Marshall et al. 2006). The model is based on realistic assumptions about the formation and evolution of four main stellar populations of the Milky Way. It allows one to simulate the stellar content along any given line of sight, and for each simulated star the photometry, kinematics, and metallicity are computed. For each population, a star formation rate history, age, and initial mass function are assumed, which leads to a distribution function in absolute magnitude, effective temperature, and age of the stars. The distribution function is assumed to be controlled by dynamical principles (Bienaymé et al. 1987) for each population and are tested by means of photometric star counts. We estimated the distances of the components distributed toward the 0 km s^{-1} feature (the dashed box in Figures 11(a)–(d)) by comparing it with the three-dimensional interstellar extinction distribution by the Besanćon model. The simulated color–magnitude diagrams are in excellent agreement with the IRSF color–magnitude diagram (Figure 23), making us confident that we can use this model to predict the distances.

The result is shown in Figure 12, which indicates that there are two extinction components toward the direction of the 0 km s^{-1}

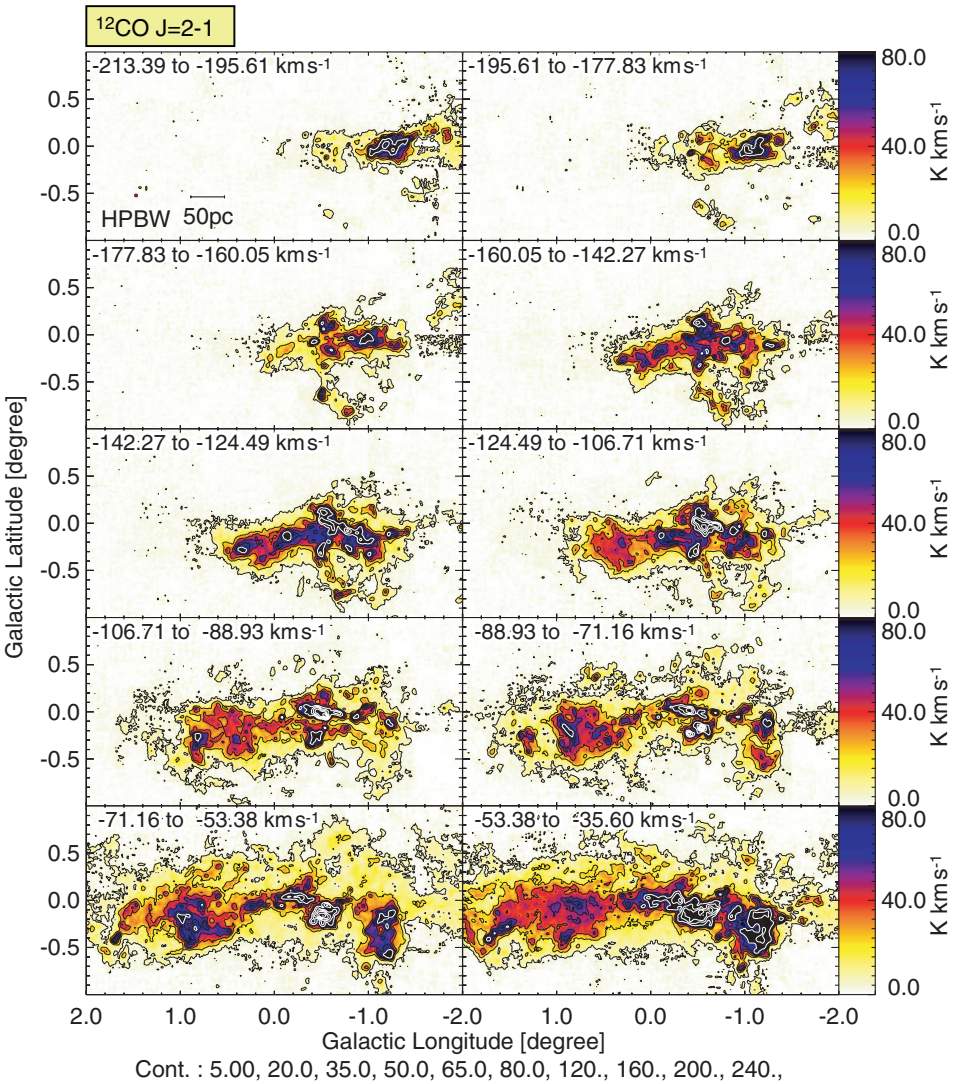

Figure 15. Velocity channel distributions of the ^{12}CO $J = 2$–1 emission integrated every 16.51 km s^{-1} between -213.4 and -35.6 km s^{-1}. The contour values are indicated at the bottom of the figure.

(A color version of this figure is available in the online journal.)

feature and ridge. One is a weak peak located at 2 kpc but, on the other hand, the other has a strong peak at around 8 kpc, the distance to the GC. We also looked at the typical distance distribution of the three-dimensional dust extinction map of Marshall et al. (2006) which shows clearly that in the direction of the 0 km s^{-1} feature and ridge most of the extinction is situated at a distance of 8 kpc. Marshall et al. (2006) also showed the excellent agreement between the dust extinction features and the CO gas, indicating the direct association between the dust and gas features. We therefore suggest that the 0 km s^{-1} feature and ridge are located in the GC. However, the latter has an intrinsic dispersion associated with the depth of the bulge itself and we adopt the distance to the 0 km s^{-1} feature and ridge as 8 kpc $\pm$2 kpc by taking into account the size of the bulge.

3.6. Summary of the Observational Results

We here summarize the present observational results with NANTEN2 as follows.

1. We have found two CO features toward the DHN at -35 km s^{-1} and 0 km s^{-1} which are extended along the DHN. The two CO features are likely associated with the DHN as suggested by the morphological correlation with the infrared nebula. Follow-up observations at three times higher angular resolutions show detailed correspondence and lend support for this association (Torii et al. 2013). The two features show velocity gradients of 0.4 km s^{-1} pc^{-1} in the same sense perpendicular to the long axis of the DHN at a distance of 8 kpc.

2. We have also found two CO ridges at the same two velocities toward the Galactic south of the CO features, that extend from the bottom of the DHN down toward the Galactic plane (Figure 5), although contamination by other features makes these ridges difficult to follow at latitudes below 0°.2 in ^{12}CO (Figure 4). We note that the CO ridges show spatial correspondence with the *Spitzer* infrared distribution within $l = -0°.2$ to 0°.2 and b above 0°.3, where contamination is not so heavy. In particular, correspondence with CO emission is good for the infrared DHN and its filament directed toward the Galactic plane (Figure 5). It is apparent that the 0 km s^{-1} ridge is connected with the 0 km s^{-1} feature, as shown in the latitude–velocity diagram (Figure 6). On the other hand, connection of the -35 km s^{-1} feature with the -35 km s^{-1}

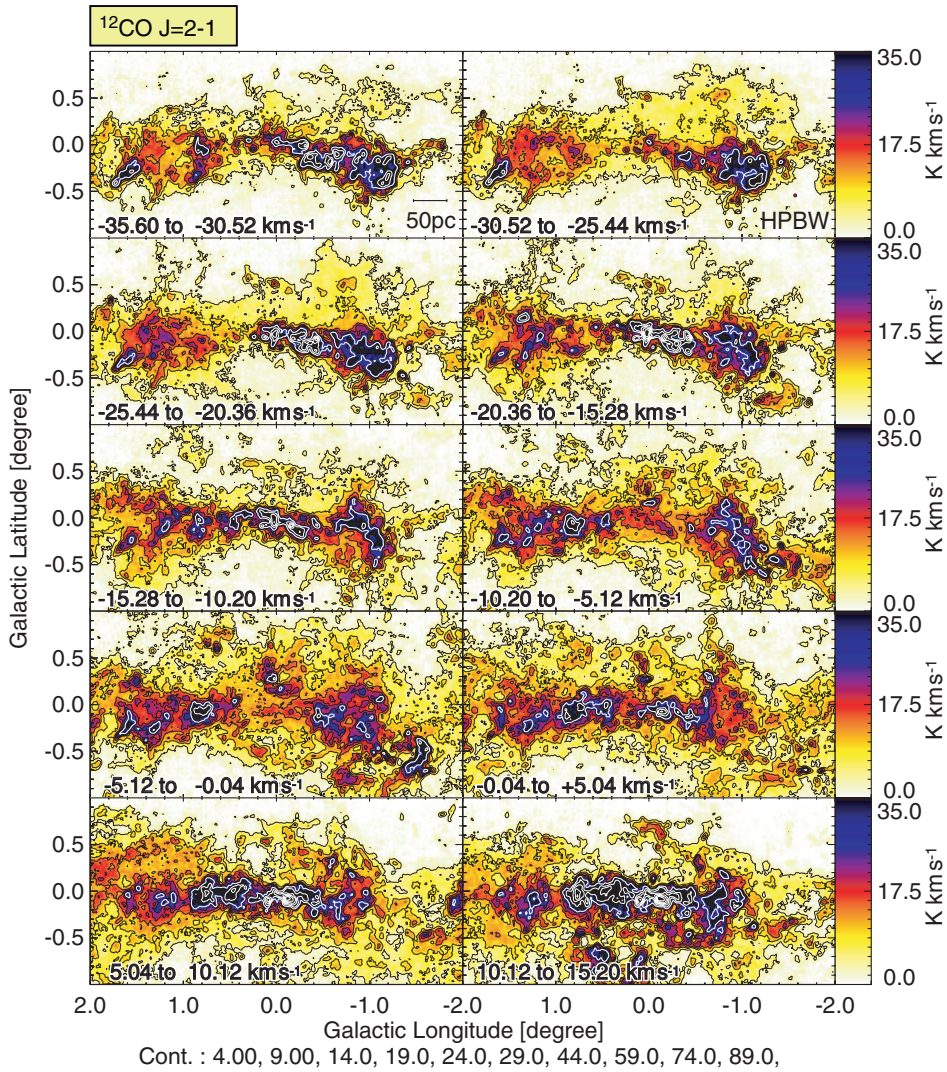

Figure 16. Velocity channel distributions of the ^{12}CO $J = 2$–1 emission integrated every 5.08 km s^{-1} between −35.6 and +15.2 km s^{-1}. The contour values are indicated at the bottom of the figure.

(A color version of this figure is available in the online journal.)

ridge is not as clear in the latitude–velocity diagram at $b = 0.^{\circ}4$–$0.^{\circ}6$ (Figure 6) as it is for the 0 km s^{-1} ridge. Nevertheless, the −35 km s^{-1} ridge has a large velocity span of 20 km s^{-1} in ^{12}CO (Figures 6(a) and 8(b)), suggesting that the ridge is located in the GC. The two CO ridges appear to be connected in space and velocity by kinematically broad CO features at $b = 0.^{\circ}5$ ("the connecting feature" in Figures 6, 7(b), 8(b) and 9(b)) and two broad features within $l = -0.^{\circ}1$–$0.^{\circ}1$ and $b = 0.^{\circ}1$ to $0.^{\circ}3$ (Figures 8(b) and (c)), suggesting that the two ridges are physically linked with each other.

3. Parts of the two CO ridges show a relatively high line intensity ratio ^{12}CO $J = 2$–1/$J = 1$–0 of 0.6–0.7, toward (l, b) = ($0.^{\circ}1$, $0.^{\circ}5$) at −35 km s^{-1} (Figure 10(a)), toward (l, b) = ($0.^{\circ}1$ to $0.^{\circ}2$, $0.^{\circ}3$ to $0.^{\circ}5$) at 0 km s^{-1} (Figure 10(b)), and (l, b) = ($-0.^{\circ}1$ to $+0.^{\circ}1$, $0.^{\circ}4$ to $0.^{\circ}5$) at between −50 km s^{-1} and +10 km s^{-1} (Figure 10(c)). The ratio is higher than that of the foreground gas, 0.3–0.5, and is likely due to the higher temperature of the molecular gas; this is consistent with our hypothesis that the ridges are located in the GC, where the molecular gas as a whole shows higher temperatures than in the Galactic disk (e.g., Morris & Serabyn 1996).

4. We have examined extinction in the K band toward the 0 km s^{-1} feature and the 0 km s^{-1} ridge and have shown that the extinction is well modeled by the Besanćon Galaxy Model, for a distance of 8 kpc ± 2 kpc to the 0 km s^{-1} ridge, which appears clearly in the star count image. This value is consistent with a location in the GC.

In summary, we suggest that all the ridges and features at −35 km s^{-1} and 0 km s^{-1} are probably located in the GC and it is possible that these ridges and features are physically linked altogether. More robust verification of their physical connection must await observations of higher-J CO transitions that are less contaminated by lower-excitation foreground gas.

4. DISCUSSION

Since the discovery of the DHN the physical and kinematical properties such as mass and velocity of the DHN have been unknown, hampering our understanding of its origin, based so far only on morphology. One suggestion is that the CND which is rotating around the super-massive black hole, Sgr A*, is driving the DHN (Morris et al. 2006). The DHN was suggested to be of magnetic origin by these authors, since its double helix distribution is similar to what is expected to be formed via

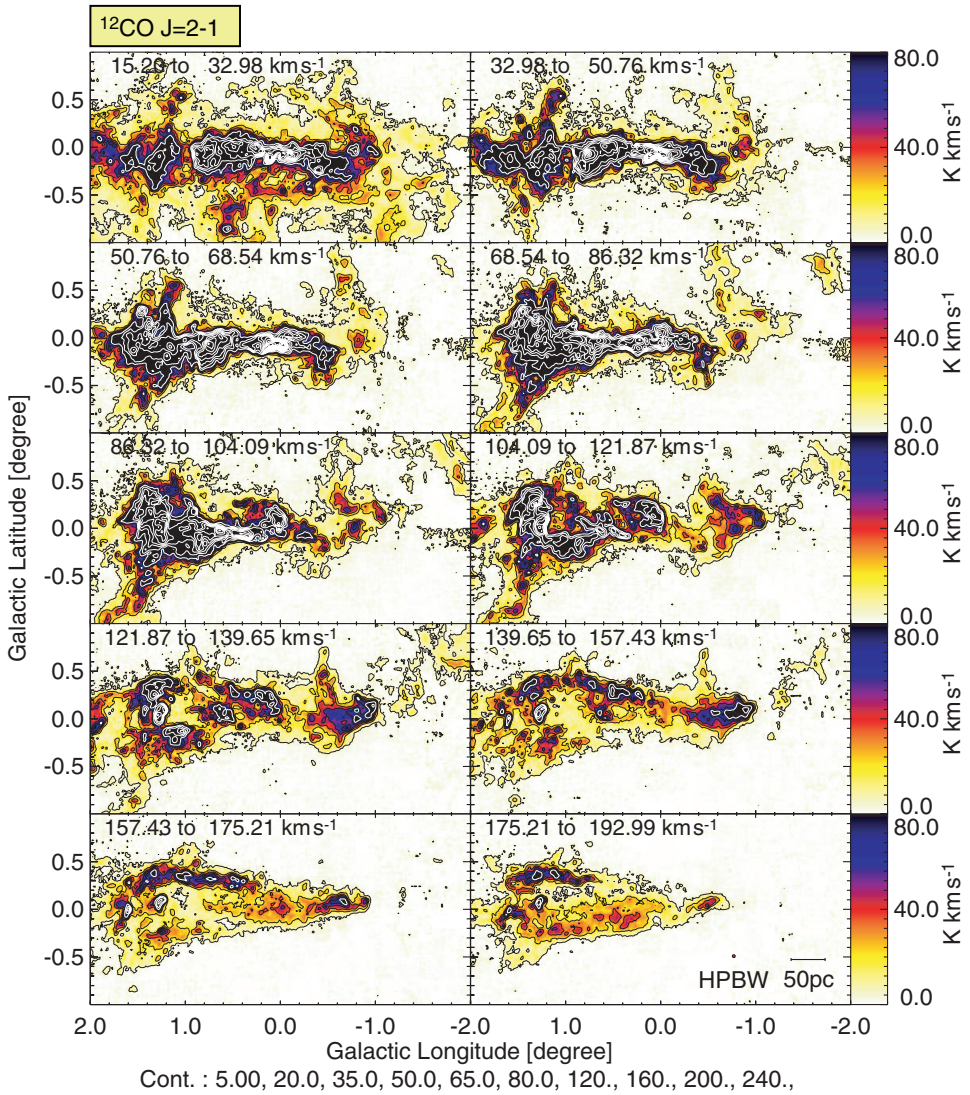

Figure 17. Velocity channel distributions of the ^{12}CO $J = 2$–1 emission integrated every 16.51 km s^{-1} between 15.2 and 193.0 km s^{-1}. The contour values are indicated at the bottom of the figure.

(A color version of this figure is available in the online journal.)

torsional Alfveń waves, which had been discussed to interpret helical CO distributions in the L1641 cloud and the ρ Oph streamers (e.g., Uchida et al. 1990, 1991). On the other hand, Law et al. (2008) and Tsuboi & Handa (2010) suggested that the DHN is located at the top of the polarized radio plume, which is driven by the Radio Arc. The origin of the Radio Arc is not yet understood and the energy that can be released from the Radio Arc is unclear; the total magnetic energy stored in the Radio Arc may be on the order of 10^{52} erg for an average field of mG and volume of 60 pc × 15 pc × 15 pc. In this scenario, the origin of the DHN shape remains unexplained.

The present CO results have opened an opportunity to explore the dynamical properties of the DHN for the first time. In the following, we compared the relevant data with the present CO images in order to elucidate the mechanisms underlying the DHN.

Figure 13(a) shows the 6cm radio continuum emission at ∼10 arcsec resolution. Figure 13(b) shows 6cm radio continuum contours overlaid on the *Spitzer* 24 μm distribution (Law 2010). It is seen that the radio continuum emission $b \geqslant 0\overset{\circ}{.}6$ traces part of the infrared distribution including the DHN and its connected filament as well as another broad filament $0\overset{\circ}{.}1$ to the west of the DHN. The radio emission toward the DHN is likely non-thermal since it is polarized (Tsuboi & Handa 2010). Similar radio continuum observations toward the whole extent of the CO ridges down to $b \sim 0\overset{\circ}{.}0$ are required to better understand the relationship of the radio continuum with the present CO distributions.

Figures 5(c) and (d) show the distributions of the *Spitzer* 24 μm emission, the radio polarized plume and the CO ridges in ^{13}CO $J = 1$–0. The locations of the Radio Arc and the CND are also compared with the *Spitzer* image in Figures 5(c) and (d). The 0 km s^{-1} ridge is along the polarized plume but becomes bent toward the CND at $b = 0\overset{\circ}{.}5$. The eastern leg of the −35 km s^{-1} ridge seems to be elongated toward the Radio Arc but the radio polarized plume is located in the east beyond the −35 km s^{-1} ridge. The western leg of the −35 km s^{-1} ridge is extended toward the CND. The leg of the −35 km s^{-1} ridge toward $(l, b) = (0\overset{\circ}{.}05, 0\overset{\circ}{.}00)$ is contaminated by the strong CO emission with large velocity width (see, e.g., Figure 5(a)). To summarize, we find that the present ridges show signs favoring association with the CND rather than with

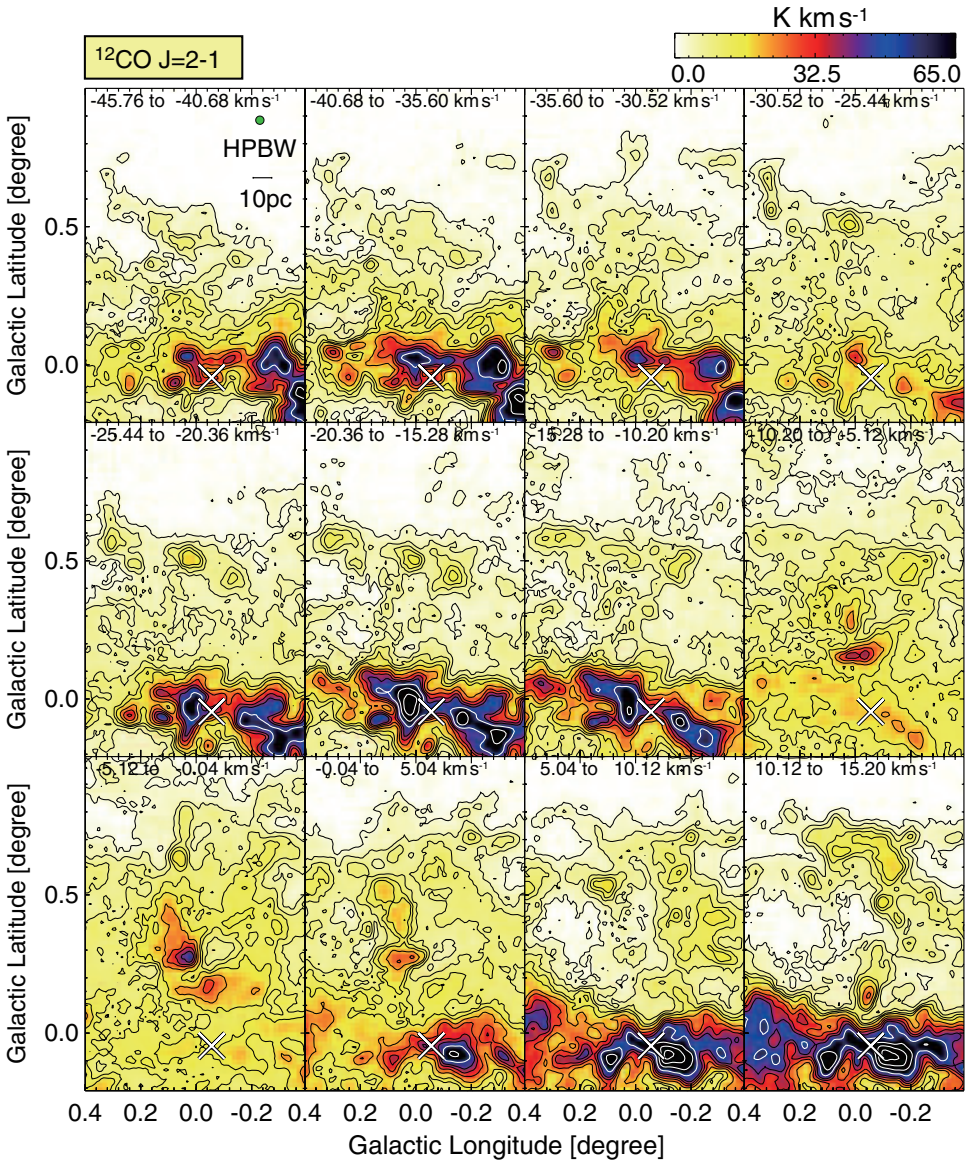

Figure 18. Velocity-channel distribution of the ^{12}CO $J = 2$–1 emission integrated every 5.08 km s^{-1} from −45.76 to +15.20 km s^{-1}. Contours are plotted at every 3.2 K km s^{-1} from 2.2 to 11.8 K km s^{-1}, every 6.5 K km s^{-1} from 15.0 to 47.5 K km s^{-1} and every 18.0 K km s^{-1} from 54.0 to 126.0 K km s^{-1}. White crosses indicate the position of SgrA*.

(A color version of this figure is available in the online journal.)

the radio polarized plume, whereas a better confirmation of the association is desirable by higher-J CO transitions with much less contamination than lower-J CO transitions.

By sensitive CO observations with NANTEN2 we have discovered at least seven filamentary CO features which extend from the CMZ nearly vertically to the Galactic plane (a fuller account will be presented by R. Enokiya et al. (2013, in preparation)). The filaments are associated with more diffuse CO halos having 10^5 $M_\odot$ surrounding the CMZ. Figure 14 gives a schematic of the filamentary CO features. The two CO ridges below the DHN are two of these CO filaments. We have shown that the observational signatures of the present CO ridges are consistent with being located in the GC (Section 3). The filamentary CO filaments have velocities from −200 km s^{-1} to 160 km s^{-1} and large linewidths of more than 60 km s^{-1} except for the present CO features. It is likely from a kinematic point of view that all of these features are located in the GC because of their large velocities and velocity spans. Two molecular filaments above Sgr C discussed in Uchida et al. (1994) seem to be associated with infrared sources, AFGL5376 and other infrared filamentary structures observed with *Spitzer* (Stolovy et al. 2006). The total mass and kinetic energy involved in all the filaments amounts to 10^6 $M_\odot$ and 10^{52} erg, respectively. Uchida et al. (1994) discussed that these filaments and the DHN are similar in shape and are of shock-related origin. Their kinematics in CO emission is, however, quite different. In particular, the peak velocities of the DHN features are −35 km s^{-1} and 0 km s^{-1}, much lower than that of the two filaments toward AFGL5376, whose velocity ranges from 40 to 160 km s^{-1}, suggesting that the DHN is of different origin from the rest. The possibility of a relation between the DHN and the other infrared filaments will be discussed separately (R. Enokiya et al. 2013, in preparation).

The CO filaments at high z around 100 pc require some energy source and mechanism for their formation against the strong stellar gravity in the inner 100 pc of the GC. Active

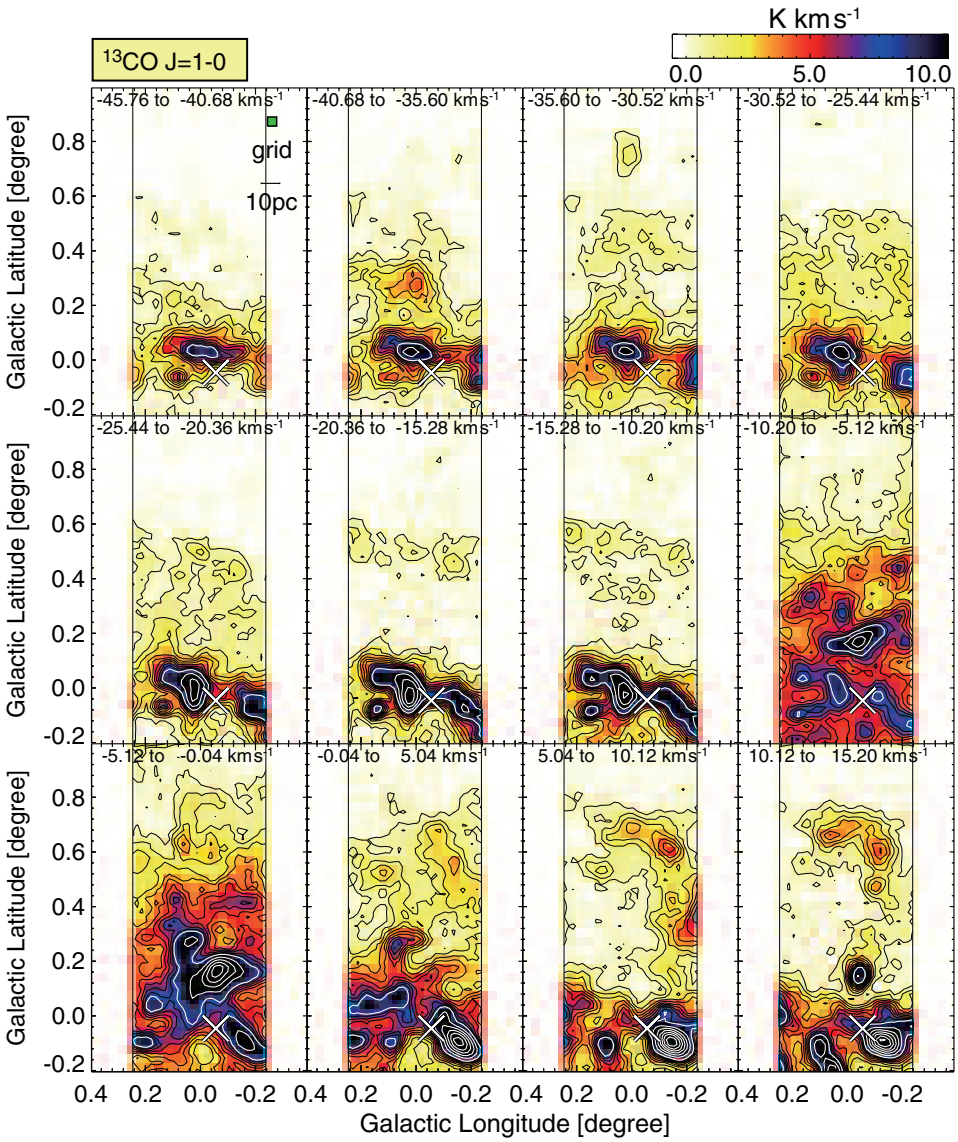

Figure 19. Velocity-channel distribution of the ^{13}CO $J = 1$–0 emission integrated every 5.08 km s^{-1} from −45.76 to +15.20 km s^{-1}. Contours are plotted at every 0.8 from 0.8 K km s^{-1} to 7.2 K km s^{-1} and every 3.0 K km s^{-1} from 8.0 K km s^{-1}. White crosses indicate the position of SgrA*.

(A color version of this figure is available in the online journal.)

high-mass star formation may provide such energy via stellar winds, supernova explosions, etc. (e.g., Crocker 2012). Except for the CO features and ridges having low velocities close to zero, the other filamentary features have velocities similar to that of the "parallelogram" in the l–v diagram at around 100–200 km s^{-1}, outside the velocity range of the Sgr A, Sgr B2, and Sgr C giant molecular clouds, whose velocity range from −50 km s^{-1} to 100 km s^{-1} (see, e.g., Figure 17). These three giant molecular clouds are known to be active in star formation, while the "parallelogram" in the l–v diagram shows no sign of active star formation (see Section 3.4). High-mass stars may possibly accelerate the gas (e.g., Crocker 2012), but the highest velocity observed, more than 100 km s^{-1}, is too large to be explained by such a process. Another possible mechanism to lift up the molecular gas is the Parker instability (Parker 1966). The three molecular loops at kpc separation from the GC, loops 1, 2, and 3, discovered by NANTEN CO observations (Fukui et al. 2006; Torii et al. 2010a, 2010b; Fujishita et al. 2009) show that the Parker instability is operating to levitate molecular gas vertically to the Galactic plane under the magnetic field of 100 μG or higher. It is probable that the magnetic field strength is even higher in the inner 100 pc than at 1 kpc of the GC, where loops 1, 2, and 3 are located. The typical kinetic energy involved in these loops is 10^{51} erg (Fukui et al. 2006) and the Parker instability offers an alternative mechanism to create the filaments except for the DHN. According to these previous works, the features created by the Parker instability show very large linewidth like 50–100 km s^{-1}, which is much larger than the velocity dispersion of the DHN. We therefore do not consider that the DHN is created by the Parker instability, whereas the other filamentary features having large linewidths are well explained by the Parker instability.

According to the above discussion, the CND seems to be a plausible candidate for the driving engine in creating the DHN via torsional Alfvénic waves as originally suggested (Morris et al. 2006). The magnetic "tower" above the central massive black hole in galactic centers is a common signature of MHD numerical simulations of a magnetized rotating nuclear disk of a galaxy and they originate from the twisted magnetic field lines around the rotating disk surrounding the central super-massive

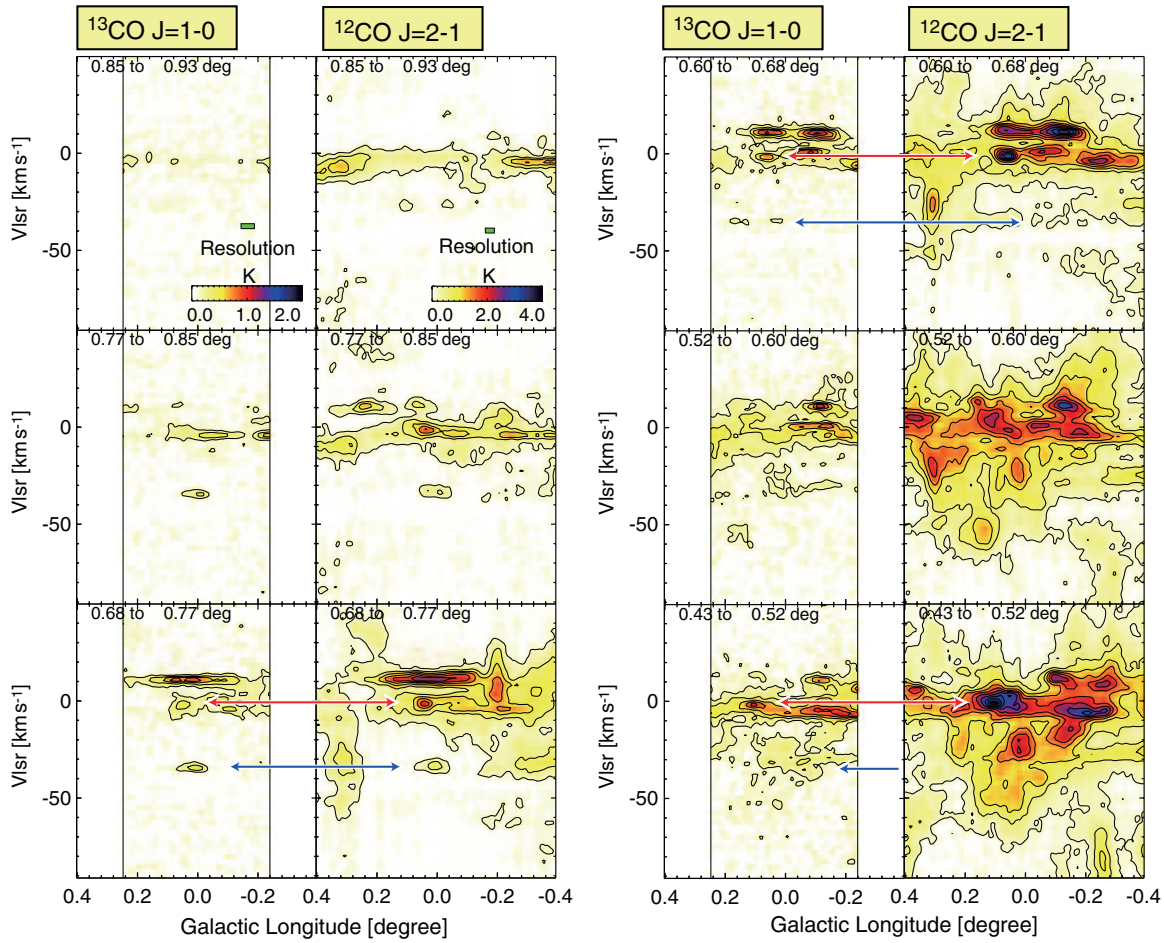

Figure 20. Latitude–velocity channel distribution of the ^{13}CO $J = 1$–0 (at the left) and ^{12}CO $J = 2$–1 emission (at the right) integrated in 0.°08 latitude intervals from 0.°43 to 0.°93. Red and Blue arrows show the 0 and -35 km s^{-1} feature/ridge, respectively.

(A color version of this figure is available in the online journal.)

black hole (e.g., Machida et al. 2009). A possible picture along this line is that magnetic fields anchored to the two diametrically opposite parts of the disk are twisted to form a double helix pattern of the magnetic fields, which creates the infrared DHN and ridges. Such a model requires realistic three-dimensional MHD numerical simulations for the appropriate parameters of the CND and should be compared with the observations in detail in the future. This is, however, beyond the scope of the present observational paper, and we simply describe a basic scenario for such a possible model below.

The model may be applied to the CO feature(s) and the CO ridge(s) as the molecular gas associated with the magnetic tower, and we show parameters for the both cases. Since the magnetic tower is hypothesized to be rising from the CND in response to magnetic pressure (Machida et al. 2009), the ambient molecular and/or atomic gas will be driven and possibly dragged by the rising magnetic field lines. We find that neutral gas in the halo may serve as the mass reservoir in the interaction. For a typical rotation speed of 80 km s^{-1} at 2 pc radius of the CND (Oka et al. 2011), the rotation period of the field lines is 0.15 Myr one rotation is supposed to form one turn of the double helix, whose length corresponds to 15 pc. This gives a total number of turns around 8 for the total length of the DHN and ridges, ∼120 pc, about 20% of which corresponds to the DHN. A rising velocity of the filament is estimated to be 100 km s^{-1} through dividing 15 pc by 0.15 Myr. The timescale of the DHN formation only is estimated to be ∼0.2 Myr for a length observed as the DHN, ∼20 pc, or 0.8 Myr–1.0 Myr ago from the current epoch, and ∼1.2 Myr if the whole system of 120 pc length is considered. We note that the observed velocity gradients in the -35 km s^{-1} and 0 km s^{-1} features are qualitatively consistent with that of the CND (Oka et al. 2011). This is interesting, even if the velocity gradient is two orders of magnitude smaller than that on the CND, because the angular momentum of the magnetic tower will be significantly lost by the interaction with the ambient gas.

Total kinetic energy of the system is estimated to be 10^{47} erg (only for the 0 km s^{-1} DHN) to 10^{51} erg (including the two velocity CO features and ridges) by considering only the lateral expanding motion perpendicular to the rotation axis of the CND. The mass accretion rate required to release such energy is roughly estimated to be $\sim 10^{-5}$ $M_\odot$ yr^{-1} at 2 pc radius in the CND for the DHN only, and $\sim 10^{-2}$ $M_\odot$ yr^{-1} for the whole features and ridges if a complete conversion of the released energy into the kinetic energy is assumed, where we take the mass of the Sgr A* to be 4×10^6 $M_\odot$ (Ghez et al. 2008; Gillessen et al. 2009). This mass accretion rate is not uncomfortably large. It is to be noted that this mass accretion rate does not directly apply to the accretion to Sgr A* itself, because most of the accreting mass in the CND will probably be ejected outward at much large radii as the magnetic tower.

We finally note that similar jet-like elongated molecular clouds are observed toward Westerlund 2 (Fukui et al. 2009; Furukawa et al. 2013), and SS433 and MJG348.5 (Yamamoto

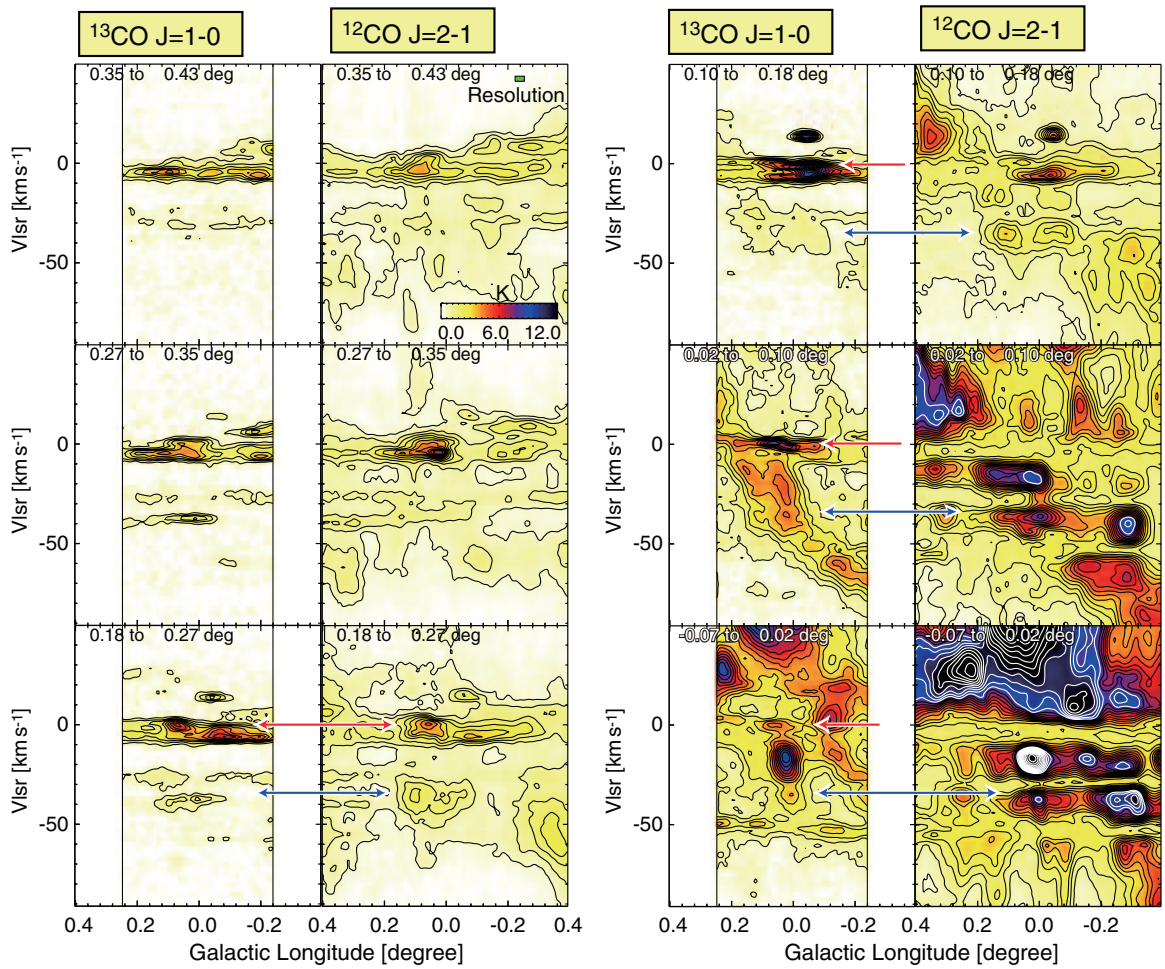

Figure 21. Latitude–velocity channel distribution of the ^{13}CO $J = 1$–0 (at the left) and ^{12}CO $J = 2$–1 emission (at the right) integrated in 0.°08 latitude intervals from −0.°07 to 0.°43. Red and Blue arrows show the 0 and −35 km s^{-1} feature/ridge, respectively.

(A color version of this figure is available in the online journal.)

et al. 2008). The possible driving source includes a compact stellar remnant like a black hole or a neutron star which may be related to the gamma-ray emission. Based on these observations it is suggested that the interaction between high-energy jet with the surrounding neutral clouds, either in molecular and/or dense atomic gas, is able to form straight and long molecular gas along the jet axis (Yamamoto et al. 2008; Fukui et al. 2009). We admit that the magnetic tower proposed here is not the high-energy jet in SS433. Nonetheless, the basic physics in the interaction shares similarities between the two in particular in the dynamical interaction with the ambient gas. Y. Asahina et al. (2013, in preparation) successfully developed MHD numerical simulations aiming at explaining the physical processes involved in these jet-like clouds. Such a model may offer a possible explanation to form the present CO features/ridges.

5. CONCLUSIONS

We have discovered two candidate molecular features associated with the infrared DHN in the distribution of the ^{12}CO $J = 2$–1, ^{12}CO and ^{13}CO $J = 1$–0 emission obtained with NANTEN2 in the GC. Two CO features at velocities of −35 km s^{-1} and 0 km s^{-1} correspond well to the infrared distribution of the DHN. This association is reinforced by follow-up observations at three times higher angular resolutions (Torii et al. 2013). We have also found two elongated CO ridges at these two velocities oriented vertically to the Galactic plane over 0.°8. The two ridges are linked by broad velocity features and are likely connected physically with each other. The physical connection between the CO DHN and the two CO ridges is possible because of the coincidence in space and velocity, while contamination by other CO features in the same direction hampers to firm establishment of an association between the two CO features and ridges. It is likely that the CO counterparts of the DHN are in the GC. An analysis of the K band extinction shows a good coincidence with the 0 km s^{-1} ridge and a modeling of the three-dimensional stellar distribution yields a distance of 8 ± 2 kpc to the 0 km s^{-1} ridge. The large velocity span of the −35 km s^{-1} ridge, ⩾ 20 km s^{-1}, favors its location in the GC. We therefore suggest that the two ridges are located in the GC. We suggest that further observations in higher J transitions of CO, etc., may provide a more convincing evidence for their locations. The molecular mass of the DHN is estimated to be $\sim 10^4$ $M_\odot$, while that of the ridges is $\sim 10^5$ $M_\odot$. The kinetic energies involved in the DHN and the ridges are roughly estimated to be 10^{47} erg and 10^{51} erg, respectively for assumed minimum velocity spans of 1–20 km s^{-1}. The placement and orientation of the ridges in ^{13}CO suggests that the 0 km s^{-1} ridge may be linked to the CND. We discuss a possibility that the DHN has its origin at the CND and was created by a magnetic phenomenon incorporating torsional Alfvén waves launched from the CND as proposed by Morris et al. (2006). If we assume the CND as

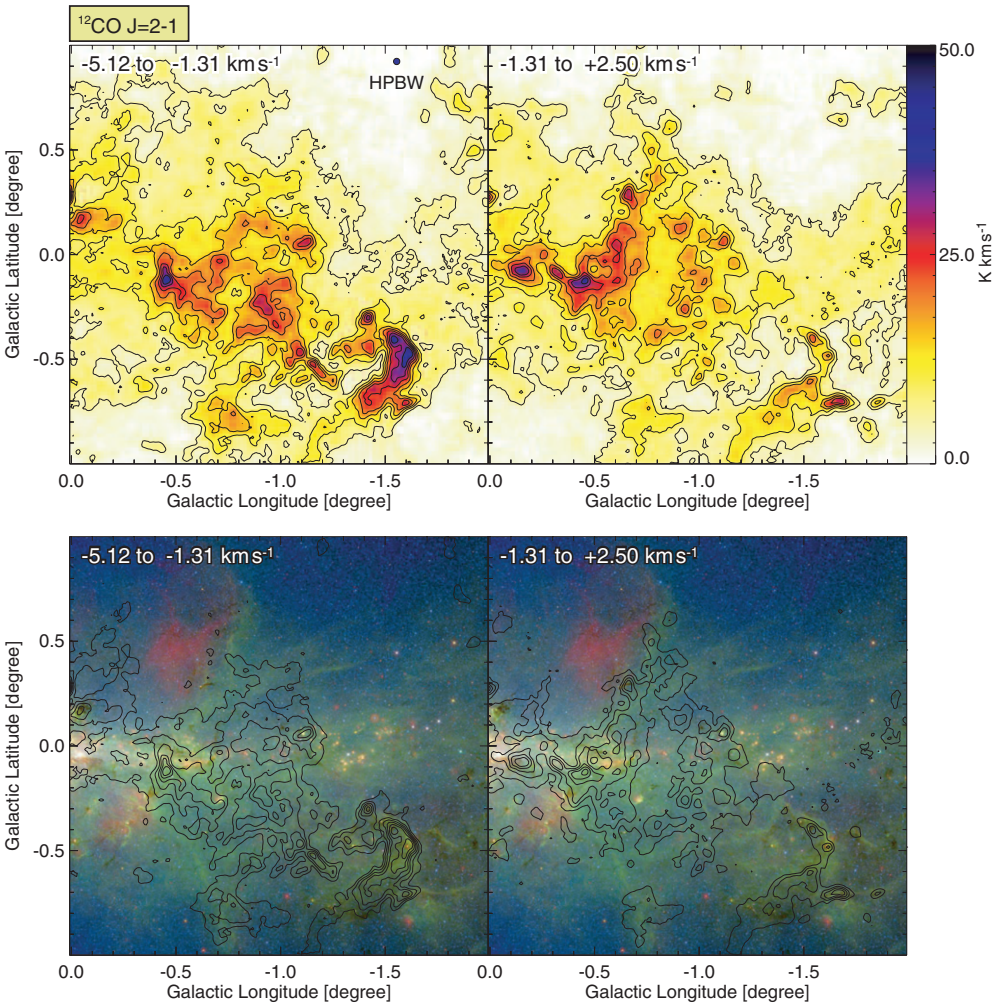

Figure 22. (a) and (b) Velocity channel distributions of ^{12}CO $J = 2$–1 emission. The integration range in $V_{\rm lsr}$ is shown in the figures. Contours are plotted at every 5 K km s^{-1} from 5 K km s^{-1}. (c) and (d) Superpositions of CO contours shown in (a) and (b) on the *Spitzer* composite images including 3.6 μm (blue), 8 μm (green) and 24 μm (red).

the origin of driving the DHN, a mass accretion rate in the order of 10^{-2} $M_\odot$ yr^{-1} to 10^{-5} $M_\odot$ yr^{-1} at 2 pc radius of the CND will explain the kinetic energy of the DHN as due to a past ejection event ∼1 Myr ago, or alternatively, the DHN and the ridges as a whole may be driven by a continuous ejection process over the last ∼1 Myr.

NANTEN2 is an international collaboration of 10 universities: Nagoya University, Osaka Prefecture University, University of Cologne, University of Bonn, Seoul National University, University of Chile, University of New SouthWales, Macquarie University, University of Sydney, and University of ETH Zurich. This work is financially supported by Grant-in-Aid for Scientific Research (KAKENHI) from Japan Society for the Promotion of Science (JSPS; Nos. 24224005, 23403001, 23006148-01, 22740119, 22540250, 22244014, and 23740149-1), young researcher overseas visits program for vitalizing brain circulation (No. R2211) from JSPS, and the Grant-in-Aid for Nagoya University Global COE Program, "Quest for Fundamental Principles in the Universe: From Particles to the Solar System and the Cosmos," from the Ministry of Education, Culture, Sports, Science and Technology of Japan (MEXT). This work is based in part on archival data obtained with the *Spitzer Space Telescope*, California Institute of Technology under a contract with NASA. Support for this work was provided by an award issued by JPL/Caltech. This publication makes use of data products from the Two Micron All Sky Survey, which is a joint project of the University of Massachusetts and the Infrared Processing and Analysis Center/California Institute of Technology, funded by the National Aeronautics and Space Administration and the National Science Foundation.

APPENDIX

Figures 15–17 show the velocity-channel distributions of the ^{12}CO $J = 2$–1. Several molecular vertical filaments and also the 0 km s^{-1} and −35 km s^{-1} ridge can be seen in these maps. Summary of these molecular filaments is shown in Figure 14. We will publish details of molecular filaments in another paper (R. Enokiya et al. 2013, in preparation). Figures 18 and 19 show the velocity-channel distributions of the ^{12}CO $J = 2$–1 and ^{13}CO $J = 1$–0 emission. They show the detailed distributions of the discovered two CO features and ridges and the connecting feature. While the ^{12}CO $J = 2$–1 emission in $|b| < 0\overset{\circ}{.}2$ is strongly affected by absorption especially at the velocity range around 0 km s^{-1}, the ^{13}CO $J = 1$–0 emission clearly describes the gas distributions not affected by absorption. Figures 20 and 21 show latitude-channel distributions of the ^{12}CO $J = 2$–1 and

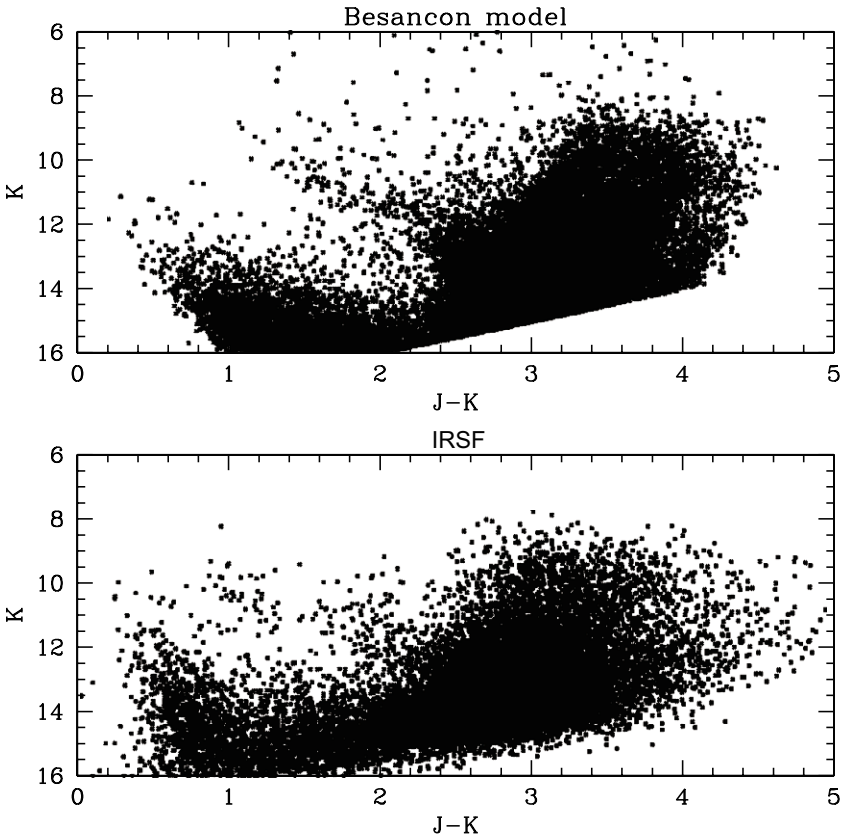

Figure 23. Comparison between the observed $J-K$ vs. K diagram (lower panel) and the synthetic color–magnitude diagram from the Besançon stellar population synthesis is model (Robin et al. 2012). The foreground branch at 2 kpc and the galactic Bulge red giant branch at 8 kpc are clearly visible.

^{13}CO $J = 1$–0 emission. Diffuse and broad velocity features seen in ^{12}CO $J = 2$–1 at (l, b, v)$\sim$ ($-0\overset{\circ}{.}2$–$0\overset{\circ}{.}2$, $-0\overset{\circ}{.}07$–$0\overset{\circ}{.}60$, -50 km s^{-1} –0 km s^{-1}) fills the interspace between two molecular ridges at v of -35 and 0 km s^{-1}. Emission from foreground clouds can be seen as narrow velocity features in these figures. Figure 22 shows velocity-channel distributions of foreground molecular cloud with high intensity ratio which corresponds to *Spitzer* filament. Figure 23 is comparison between color–magnitude diagram of the Besanćon model and observational data of IRSF.

REFERENCES

Bienaymé, O., Robin, A. C., & Crézé, M. 1987, A&A, 186, 359
Binney, J., Gerhard, O. E., Stark, A. A., et al. 1991, MNRAS, 252, 210
Crocker, R. M. 2012, in IAU Symp. 284, The Spectral Energy Distribution of Galaxies, ed. R. J. Tuffs & C. C. Popescu (Cambridge: Cambridge Univ. Press), 371
Crocker, R. M., Jones, D. I., Melia, F., Ott, J., & Protheroe, R. J. 2010, Natur, 463, 65
Dobashi, K. 2011, PASJ, 63, S1
Fujishita, M., Torii, K., Kudo, N., et al. 2009, PASJ, 61, 1039
Fukui, Y., Furukawa, N., Dame, T., et al. 2009, PASJ, 61, 23
Fukui, Y., Yamamoto, H., Fujishita, M., et al. 2006, Sci, 314, 106
Furukawa, N., Ohama, A., Fukuda, T., et al. 2013, ApJ, submitted
Ghez, A. M., Salim, S., Weinberg, N. N., et al. 2008, ApJ, 689, 1044
Gillessen, S., Eisenhauer, F., Fritz, T. K., et al. 2009, ApJ, 707, 114
Kudo, N., Torii, K., Machida, M., et al. 2011, PASJ, 63, 171
LaRosa, T. N., Nord, M. E., Lazio, T. J. W., & Kassim, N. E. 2004, ApJS, 607, 302
Law, C. J. 2010, ApJ, 708, 474
Law, C. J., Yusef-Zadeh, F., & Cotton, W. D. 2008, ApJS, 177, 515
Machida, M., Matsumoto, R., Nozawak, S., et al. 2009, PASJ, 61, 41
Marshall, D. J., Robin, A. C., Reylé, C., et al. 2006, A&A, 453, 635
Molinari, S., Bally, J., Noriega-Crespo, A., et al. 2011, ApJL, 735, L33
Morris, M., & Serabyn, E. 1996, ARA&A, 34, 645
Morris, M., Uchida, K., & Do, T. 2006, Natur, 440, 308
Morris, M., & Yusef-Zadeh, F. 1985, AJ, 95, 2511
Oka, T., Nagai, M., Kamegai, K., & Tanaka, K. 2011, ApJ, 732, 120
Parker, E. N. 1966, ApJ, 145, 811
Robin, A. C., Marshall, D. J., Schultheis, M., & Reylé, C. 2012, A&A, 538, 106
Sawada, T., Hasegawa, T., Handa, T., et al. 1999, AdSpR, 23, 985
Sofue, Y. 1995, PASJ, 47, 527
Sofue, Y., & Handa, T. 1984, Natur, 310, 568
Stolovy, S., Ramirez, S., Arendt, R. G., et al. 2006, JPhCS, 54, 176
Takahashi, K., Nozawa, S., Matsumoto, R., et al. 2009, PASJ, 61, 957
Torii, K., Enokiya, R., Hasegawa, K., et al. 2013, ApJ, submitted
Torii, K., Kudo, N., Fujishita, M., et al. 2010a, PASJ, 62, 675
Torii, K., Kudo, N., Fujishita, M., et al. 2010b, PASJ, 62, 1307
Tsuboi, M. 1999, ApJS, 120, 1
Tsuboi, M., & Handa, T. 2010, ApJ, 719, 177
Uchida, K. I., Morris, M. R., Serabyn, E., & Bally, J. 1994, ApJ, 421, 505
Uchida, Y., Fukui, Y., Minoshima, Y., Mizuno, A., & Iwata, T. 1991, Natur, 394, 140
Uchida, Y., Mizuno, A., Nozawa, S., & Fukui, Y. 1990, PASJ, 42, 69
Yamamoto, H., Ito, S., Ishigami, S., et al. 2008, PASJ, 60, 715
Yusef-Zadeh, F., Hewitt, J. W., & Cotton, W. 2004, ApJ, 155, 421
Yusef-Zadeh, F., Morris, M., & Chance, D. 1984, Natur, 310, 557